Radiative Energy Loss of Muons in the MINOS Far Detector

A Thesis submitted to the

Faculty of Graduate School of the University of Minnesota Duluth

by

Prabhat Bhattarai

In partial fulfillment of the requirements for the

degree of Master of Science

[July 2010]

Abstract

Higher energy (>100 GeV) muons lose their energy preferentially through radiative methods such as Bremsstrahlung, Pair-production and Photo-production. Because the radiative loss of the energy is a stochastic process, it is hard to select muons which lose their energy through the radiative methods. I will present methods of selecting the highest energy muons in MINOS, looking for radiative energy losses.

The MINOS far detector is an underground detector. Since August 2003 the MINOS Far Detector has been collecting the underground muons [1]. The detector receives mostly high energy muons because most of the low energy cosmic muons are absorbed by the rocks in the path. They lose energy in the detector in the form of showers of particles and radiation.

To study the cosmic muons reaching the MINOS Detector I have used cosmic ray Monte Carlo simulated data. I applied a number of cuts in the simulated data to select high energy muons. Then I compared the Monte Carlo simulated data with the MINOS far Detector data. I found a high correlation in the data with the correlation coefficient of 0.95 or more depending on the variable I chose to compare. The high correlation suffices to tell that the cuts chosen in the Monte Carlo simulated data are applicable in the case of the Detector data also.

Acknowledgements

Thanks for mother nature not only for creating ample space to think and analyze but also for bringing me upto this workplace from diametrically opposite corner of the globe.

I first of all wish to thank prof. Alec Habig, my thesis adviser, who not only made this work possible, but through his constant encouragement kept me on the right track. His continuous suggestions and ideas made the work richer, both in content and form. I am grateful to Jeff de Jong for his uninterrupted help in technical issues of programming.

I would like to thank my parents, brothers, sisters for their continuous encouragements. My wife, Sharmila helped me a lot in every possible way. I would like to thank her for her patience and support.

I am grateful to Department of physics for its support and also grateful to all faculties and staffs of the department for support. I am specially grateful to prof. Richard Gran for his insight towards the subject matter.

I thank to friends Arjun, Ghaneshwar, Dharma and Puskar for constant encouragement and suggestions.

Contents

List of Figures

List of Tables

Chapter 1

Introduction

Interstellar particles that impinge upon the earth are called “cosmic rays”. In 1937, while measuring the energy loss of particles occurring in cosmic ray shower, Anderson and Neddermeyer found the signature of particles having unit charge, mass larger than electron, but much smaller than that of proton [2]. The particle was later called the “muon”. Muons are nearly stable and have a small cross section for interactions, so they are very penetrating [3]. Muons are also called the “penetrating component” of cosmic rays. Because they are charged, they are relatively easy to detect.

1.1 Cosmic Ray Muons

Almost all muons found on the surface or inside the earth are produced when high energy hadronic cosmic rays collide with the particles on the earth’s atmosphere [4]. The collision occurs at high altitudes. The collision produces pions(π) and kaons(K); some of them decay into muons(μ). The hadronic parents are charged particles. Protons are the most abundant in the showers of particles. These particles originate from distant stars or galaxies. Thus, knowledge of the direction of such rays could possibly help to point out the point source of those particles. However, the stars and galaxies have non- uniform large (*several microgauss*) magnetic fields which lead to change in the direction of the charged particles. During the travel the cosmic particles bend repeatedly. Consequently, the direction from which they arrive on the earth’s surface bears little or no relation to the source of the rays.

Since the discovery of the cosmic rays the muon, elementary particle muons have become a fascinating

and exotic particle, which can be an objective and/or tool for fundamental physics and applied science. In particular, after intense beams of muons became available using particle accelerators in 1960, the field of scientific research using muons has been growing year by year [5]. Three major unique features of the muons have formed the basis of all muon-related scientific researches: (1) unique mass, μ^- is like heavy electron and μ^+ is like light proton; (2) radioactivity with polarization phenomena; and (3) the electromagnetic interaction nature with matter without strong interaction. Much research is going on to use the unique features of the muons in applied science. In these applications, we note that muons may be the key particles to provide answers to the basic problems associated with possible crises in human life in the twenty-first century, namely, a shortage in energy resources (for example, use of muon catalyzed fusion reaction), the need for more information on the biological functioning on the human body (for example, use of muonic atom X-ray), and the need to prevent natural disasters, such as volcanic eruptions and earthquakes [5].

1.2 Energy Loss of Muons

Muons propagating in matter are subject to energy loss. Low energy muons (smaller than 100 GeV), lose their energy mostly through mechanisms like atomic excitation and ionization. But the high energy muons (Energy $>$ 100 GeV) lose their energy through stochastic radiative methods such as electron-positron pair production, bremsstrahlung and photo-nuclear interaction [6]. Details of the energy loss mechanisms are included in chapter 2.

1.3 History of The Bremsstrahlung

X-rays were discovered by W. C. Röntgen in 1895, but the separate study of the two components, the characteristic line spectrum and the continuous spectrum, started only 18 year later [7]. For the continuous spectrum Sommerfield proposed the name bremsstrahlung (meaning braking radiation) with the approval of Röntgen himself. Although the coincidence experiment between emitted photons and outgoing electrons had been suggested as early as 1932 by Scherzer, the first measurement of the elementary bremsstrahlung process have been performed by Nakel beginning in 1966, those of the elementary process of electron-electron bremsstrahlung by Nakel and Pankau beginning 1972 [7].

Theoretical investigations of the bremsstrahlung process have followed the general developments in physics. Initial attempts were on the basis of classical electrodynamics. Semi-classical calculations of

Kramers in 1923 and of Wentzel made use of the correspondence principle. The first quantum- mechanical cross-section formulae for the elementary process were derived in 1931 by Sommerfeld in the non-relativistic dipole approximation including retardation. With the advent of the Dirac theory Bethe and Heitler achieved in 1934 the first relativistic calculation of bremsstrahlung in the Born approximation. For details see chapter 2. A significant amount of quality research on pair-production of electron and other leptons such as muons has been carried out since the discovery of Dirac's equation in 1928. Around 1972 much work on bremsstrahlung and pair-production of electron and muon were done at the Stanford Linear Accelerator Center (SLAC) [8]. For theoretical calculations, the pair-production is related to the bremsstrahlung problem by the substitution rule. The calculation of the pair production cross section is trivial once we know how to calculate the bremsstrahlung [8]. So, both of the physical phenomena are being studied simultaneously.

1.4 The MINOS Experiment

The Main Injector Neutrino Oscillation Search (MINOS) is a long-baseline neutrino oscillation experiment. It consists of three major components: (1) A muon neutrino (ν_μ) beam, neutrinos at the Main Injector (NuMI), provided by the Main Injector at Fermi National Accelerator Laboratory in Batavia, IL; (2) the Near Detector about 1 km from the neutrino beam target, to detect the initial neutrino flux and; (3) the Far Detector in Soudan, MN, to observe the final neutrino flux. The muon neutrino (ν_μ) is produced from NuMI beam just before it come across the Near Detector. After leaving the signature of its presence in the Near Detector, it starts a journey through underground rocks. Making trip of 735 km it reaches to the Far Detector. In the long distance from Near to Far Detector, the muon neutrinos get the opportunity to oscillate to one of the other types of neutrinos, electron or tau. The ν_μ flux (number per unit time over the entire beam) at the Far Detector is predicted to be about half of that seen at the Near Detector, and a clearer image of neutrino oscillations will be produced [1].

Although the main aim of the MINOS detectors is to search for the evidence of neutrino oscillation, the detectors are sensitive enough to detect the cosmic muons. Moreover, the location of the Far Detector is more suitable for the study of high energy cosmic muons because the low energy muons are absorbed by the rocks before they reach the Far Detector (see Ch. 3).

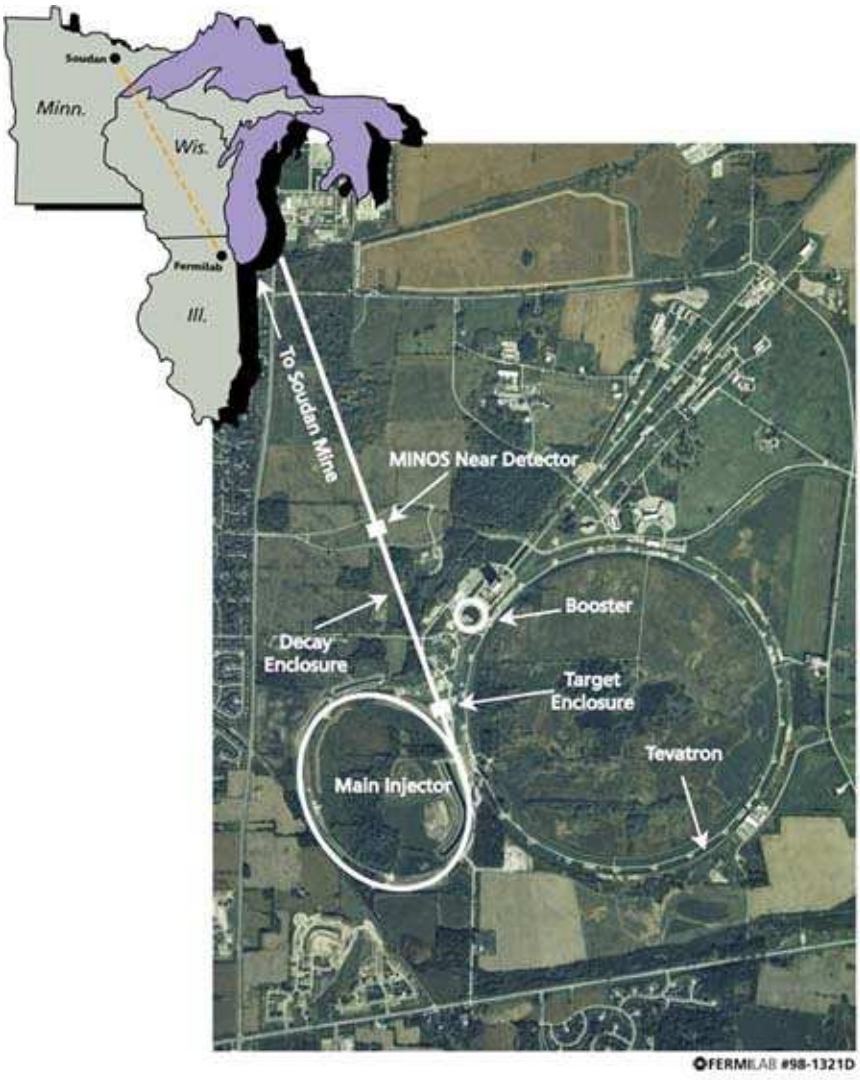

Figure 1.1: The path of the neutrino beam from Batavia, IL; to Soudan, MN. Also, the Main Injector and Tevatron on the Fermilab campus are shown in an aerial photograph.

The MINOS collaboration is an international effort, with major funding coming from the U.S. Department of Energy, the U.S. National Science Foundation, Great Britain's Science and Technology Facilities Council, and the State and University of Minnesota. MINOS institutions cover five countries over three continents, and have representation in both hemispheres.

1.5 The Goals of this Analysis

The MINOS Detectors are sensitive to cosmic muons. The most useful parameters such as momentum and energy of muons are estimated using the measurements: (1) bending of charged muons in magnetic field; and (2) stopping length of the muons by the materials of the detector. However, the error in measurement of momentum becomes large when the high energy muons pass the detector without bending by the magnetic field of the detector. Similarly, because of stochastic radiative energy loss mechanisms such as bremsstrahlung and pair-production, a large error is associated in the estimation of the energy. So a method of selecting high energy muons is difficult. The main goal of this analysis is to select high energy muons from the chunk of muons in the large energy range.

To accomplish the goal at first giving the same environment of the Detector data with known energy simulated data is created using a method called Monte Carlo (MC). In the MC data, we know the exact value of many parameters such as energy momentum etc. So, using the MC simulated data, different parameter values (cuts) are decided to select high energy events. In the next step the MC data and the data produced from the Detector are compared. If the distributions of MC data and the Detector data are similar, the cuts applied in MC data to select high energy muons in the MC data can also be applied in the Detector data.

To accomplish the goal, I have updated the cuts decided by predecessor in the MC data. Also, I have worked for the comparison between the MC data and the Detector data, and helped reprocess all the cosmic ray data in both Near and Far Detectors.

Chapter 2

Theory

From the interaction of high energy hadrons with the atmospheric elements muons are born. The probability of the birth of a muon depends upon the nature and energy of the hadrons as well as the nature of the target particle. The life of the produced muon is very short. However, because the muons are relativistic, they are able to reach the surface of the earth. Muons that reach the detector (see Ch.3) interact with the detector nuclei as well as its electrons. The result is the loss of energy. The energy loss occurs through number of ways such as bremsstrahlung, pion production, photo disintegration, ionization etc.

2.1 The Cosmic Rays

Cosmic rays are the charged particles that reach the Earth from interstellar space. They are ionized nuclei -about 90% protons, 9% alpha particles and the rest the heavier nuclei [3]. Cosmic ray particles hit the Earth's atmosphere at the rate of about 1000 per square meter per second. Most of the cosmic rays are relativistic, having energies comparable to or somewhat greater than their masses. A very few of them have ultra-relativistic energies greater than 10^8 TeV.

Where do such cosmic rays come from? How are they accelerated to such high energies? There are are many such questions which are not yet fully answered. However, it is understood that nearly all of the cosmic rays come from outside the solar system but from within the galaxy [3]. Very few of the particles originate from the sun.

2.1.1 Cosmic Ray Muon

Production of Muons

Muons are unstable elementary particles of two charge types (positive μ^+ and negative μ^-) having a spin $\frac{1}{2}$, an unusual mass intermediate between the proton mass and the electron mass ($\frac{1}{9}m_p$, $207m_e$) and 2.2 μ s lifetime [5]. Electric charge of μ^+ and μ^- is +1 and -1 respectively. Muons are mostly decay products of pion and kaons. Pion and kaon have short life times, 2.6×10^{-8}s and 1.2×10^{-8}s respectively. Because of this short life, they decay into muon neutrinos and photons:

$$\pi^{\pm} \rightarrow \mu^{\pm} + \nu_{\mu}(\bar{\nu}_{\mu}) \ \ (\sim 100\%) \tag{2.1}$$

$$\pi^{0} \rightarrow 2\gamma \ \ (\sim 98.8\%) \tag{2.2}$$

$$K^{\pm} \rightarrow \mu^{\pm} + \nu_{\mu}(\bar{\nu}_{\mu}) \ \ (\sim 63.5\%) \tag{2.3}$$

In the decay equations [3], the figure in parenthesis indicates the branching ratio.

Decay of Muon

As the life time of thus produced muon is also small (on the order of 10^{-6}s), the muons decay into electrons (e^-), positrons (e^+), neutrinos (ν) and anti-neutrinos ($\bar{\nu}$) [5].

$$\mu^{\pm} \rightarrow e^{\pm} + \bar{\nu}_{\mu}(\nu_{\mu}) + \nu_{e}(\bar{\nu}_{e}) \ \ (\sim 100\%) \tag{2.4}$$

The cosmic muons are produced in upper atmosphere. As they come toward the earth some of them disintegrate in flight. If they are such short lived, we would not expect such a large flux ($9.56\times10^{-3}\mathrm{cm}^{-2}\mathrm{s}^{-1}\mathrm{sr}^{-1}$, at a rigidity > 0.247(GV)) of muon on the earth surface and underground [6]. However, relativity plays a significant role because of time dilation, moving objects decay more slowly, resulting the larger flux of undecayed muon at the earth's surface [9].

Interactions of Muons with Matter

The muons belong to the lepton family of particles, along with electron, the tauons, and their corresponding neutrinos (ν_e, ν_μ, ν_τ). The muons interact with other particles and matter through both electoromagnetic

(EM) and weak interactions. These two interactions are unified into an "electroweak" interaction. The interaction between the muons and other particles, such as nuclei, nucleons, or quarks, system mainly from EM and weak interaction, and hence the EM properties of strongly interacting multi-quark stem can be probed by very-high-energy (> GeV) muons [5].

A low energy muon is moderately relativistic. It loses energy in matter primarily by ionization and atomic excitation. The mean rate of energy E loss per unit distance (x) (also called stopping power) is given by the Bethe-Bloch equation [10].

$$-\frac{dE}{dx} = Kz^2\frac{Z}{A}\frac{1}{\beta^2}\left[\frac{1}{2}ln\frac{2m_ec^2\beta^2\gamma^2T_{max}}{I^2} - \beta^2 - \frac{\delta(\beta\gamma)}{2}\right] \tag{2.5}$$

Where K is a constant defined as $4\pi N_A r_e^2 m_e c^2/A$,A being another constant measured in g/mol^{-1}. Further, Z is atomic number of absorber(target), e is the charge of incident particle, I is mean excitation energy in eV, T_{max} is the maximum kinetic energy that can be imparted to free electron in single collision, and $\delta(\beta\gamma)$ is density effect correction to ionization energy loss. For the low energy (<100 GeV) muons, the Bethe-Bloch equation well describes the energy loss of muons in the material. At higher energies, radiative effects begin to be important. The limit of energy within which the Bethe-Bloch equation holds depends on the atomic number Z of the target material.

At higher energy the mean rate of loss of energy is approximated as

$$-\frac{dE}{dx} = a(E) + b(E)E \tag{2.6}$$

Where $a(E)$ is the ionization energy loss (in first approximation 2 MeV per g/cm^2) given by Bethe-Bloch equation 2.5 and $b(E)$ is the sum of e^+e^- pair production, bremsstrahlung and photonuclear contributions [10] [11]. For rock b is roughly 4×10^{-6}. The critical energy for muon is the energy ε at which ionization energy equals radiation energy loss. That is $\varepsilon = a/b \backsimeq 500\,\text{GeV}$. The energy loss is dominated by radiation when E $\gg \varepsilon$ and by ionization when E $\ll\varepsilon$. The minimum energy for a muon to penetrate a depth X is given by

$$E_\mu^{min} = \varepsilon\,[exp\,(bX) - 1] \tag{2.7}$$

At small column depths, $X \ll 1/bg/cm^2$ muons lose energy mostly by ionization, and $E_\mu^{min} \backsimeq aX$. At big depths, $X \gg 1/bg/cm^2$, the spectrum has an almost constant shape of $E_\mu \backsimeq \varepsilon$ and steepens above that energy [11]. The qualitative behavior of the shape of the depth of intensity curve can also be given by the

power law $E = KE_{\mu}^{-\alpha}$. Figure 2.1 shows the contribution of the three radiative processes to the loss of energy of muons.

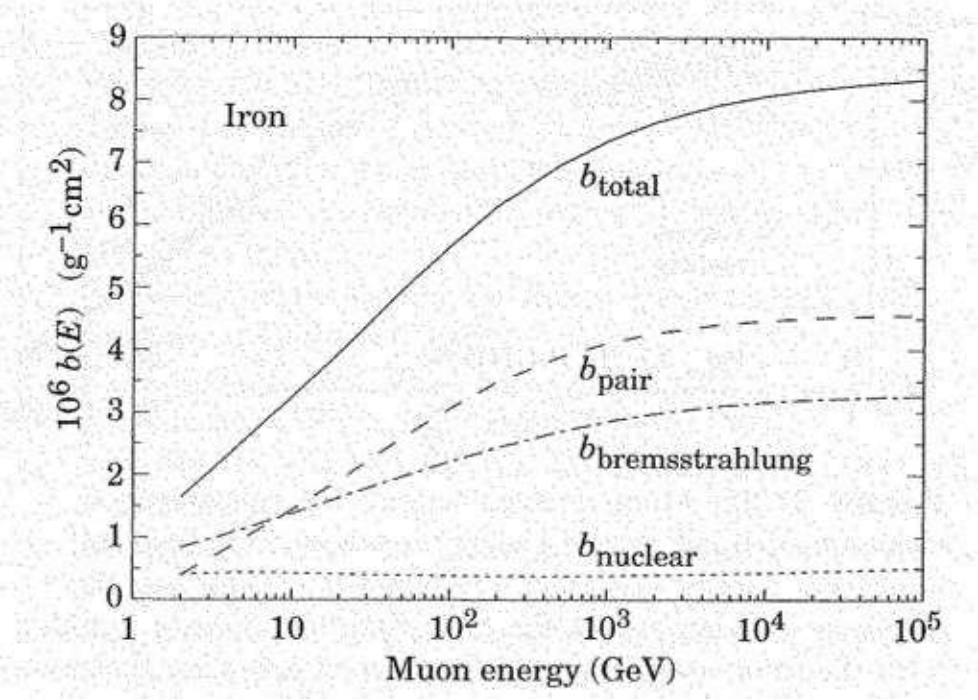

Figure 2.1: Contributions to the fractional energy loss by muons in iron due to e^+e^- pair production, bremsstrahlung, and photonuclear interactions. It does not include the post-Born corrections to the cross section for direct pair production from the atomic electrons.. [10].

The cosmic muons those pass through the rock of about 1 km, are mostly high energy muons. Therefore, in the deep underground detectors the radiation processes such as bremsstrahlung, pair production and photonuclear reactions are dominant.

2.2 Process of Energy loss of Muons

2.2.1 Ionization

As a muon passes through matter it ionizes the matter in the path. In this process it loses its energy. The rate of energy loss is given by Bethe-Bloch relation Eq. 2.5 on the facing page. Mostly low energy muons lose energy through this mechanism.

2.2.2 Bremsstrahlung

What is Bremsstrahlung

Charged particles interact with the electromagnetic field of the atom and generate photons. This process of emission of a photon in the scattering of a charged particle from an atom is called Bremsstrahlung. During the scattering of charged particle it accelerates, therefore, the Bremsstrahlung is also called the "braking radiation" [7] [11] [12].

The main force acting on the incident charged particle by the atom and leads to bremsstrahlung emission is the Coulomb field of the nuclear charge. The effect of the atomic electron is two fold: on one hand, the atomic electrons screens the Coulomb field of the nucleus as a static charge distribution and reduces the cross section for the bremsstrahlung. On the other hand, the atomic electrons act as individual particles and the bremsstrahlung process may take also take place in the collision with an atomic electron which then absorbs the recoil momentum and is ejected. In the case of bremsstrahlung of electron, this is called electron-electron bremsstrahlung. However, the cross section of muon-electron bremsstrahlung is small because muons are heavier that electrons by a factor of $\sim$200.

Basic Formulation of Bremsstrahlung

Consider a charged particle of mass m and charge qe moving along the x-axis and scattered by an atom of nuclear charge Z. The transfer of momentum in the scattering is

$$\Delta p = \int F\,dt \tag{2.8}$$

The force F is given by $qeE(r)$, where $E(r)$ is the electric field of the nucleus. The position at some instant $r(t)$ is known because we know velocity v. Assuming the change is v is very small and resolving the electric field in x and y component, we get

$$\Delta v = \frac{\Delta p}{m} = \int_{-\infty}^{\infty} \frac{qeE_y}{m} dt; \tag{2.9}$$

where the integral of E_x vanishes. If b is the closest distance of approach (also called the impact parameter) then the above integral yields

$$\Delta v = \frac{2qe^2Z}{mvb} \tag{2.10}$$

The radiation intensity I resulted from the change in velocity.So the radiation due to accelerated particle is given by

$$I = \frac{2e^2(\Delta v)^2}{3\pi c^2} \tag{2.11}$$

To find the total energy **E** radiated by a charge over all b and all the frequencies ω is

$$\frac{d\mathbf{E}}{dx} = N \int\int 2\pi I b \; db \; d\omega = \frac{16NZ^2e^6q^4}{3hc^3m}; \tag{2.12}$$

where N is number density of nuclei of target material. The above calculation of the rate of loss of energy through bremsstrahlung does not consider relativistic effects. As the incident charged particle becomes smaller and smaller and the particle's velocity grows larger and larger, relativistic effects must be accounted for to predict the behavior of the bremsstrahlung. After including relativistic effect Eq. 2.12 takes the form of [12]

$$\frac{d\mathbf{E}}{dx} = \frac{16NZ^2e^4q^2}{3hc^3m}\mathbf{E} \; ln\left(\frac{192\lambda}{Z^{1/3}}\right) \tag{2.13}$$

In this equation λ is a constant close to unity. From this equation it is clearly seen that the rate of loss of energy through the bremsstrahlung depends on the mass of the incident particle m, the atomic number of target Z, the number density of the nuclei of the target (a parameter closely related to density) N and the energy of the incident particle **E**. As the radiative loss is proportional to the energy of particle, it is not important for low energy particles. Also, the bremsstrahlung is inversely proportional to mass. Which indicates that the bremsstrahlung behavior is strong for relativistic tiny particles like electrons, muons, pions etc.

In the case of the MINOS experiment, high energy cosmic muons pass through the Steel detector producing the bremsstrahlung.

Cross-Section of Bremsstrahlung

The probability of bremsstrahlung event is given by the cross-section. The differential cross-section of muon bremsstrahlung in units of $cm^2/(g \times GeV)$ is given by [11]

$$\frac{d\sigma_{br}}{du} = \alpha \left(2Zr_e \frac{m_e}{m_\mu}\right)^2 \frac{1}{u}\left[\frac{3}{4}(1-u)+u^2\right]\xi(\delta); \tag{2.14}$$

where, $u = \frac{emitted\ \ photon\ energy}{total\ \ initial\ energy\ of\ \ muon} = \frac{\mathbf{E}-\mathbf{E}'}{\mathbf{E}}$; α is the fine structure constant with approximate value of 1/137 and; m_e and m_μ are masses of electron and muon respectively. The term $\xi(\delta)$ addresses the screening effect of the electron cloud around the atom. It is given by

$$\xi(\delta) = ln\left[f_n \frac{m_\mu}{m_e}\frac{189Z^{-1/3}}{1+(\delta/m_e)\sqrt{e}189Z^{-1/3}}\right]$$

The quantities involved are: $\delta = \frac{m_\mu^2 u}{2\mathbf{E}(1-u)}$, $\sqrt{e} = 1.648$ and f_n is a function of atomic number of target nuclei.

2.2.3 Pair Production

Direct pair-production is a process in which the muon emits a virtual photon and the virtual photon produces and electron-positron pair. In this process a photon is photon disappearance and appearance of two particles occurs simultaneously.That is, in pair production muon emits the pair of electron and positron. For high energy muons this is one of the important source of emission of energy.

Basics Formulation of Pair Production

Consider a photon of frequency ω emitting two particles; a positron e^+ and an electron e^- with respective momenta p_p and p_e and kinetic energies T_p and T_e . The relativistic conservation equations are written as: [12]

$$\begin{aligned}
\hbar\omega &= T_e + T_p + 2mc^2 \\
\frac{\hbar\omega}{c} &= p_e\cos\alpha + p_p\cos\beta \\
0 &= p_e\sin\alpha - p_p\sin\beta \\
p_e^2c^2 &= T_e(T_e+2mc^2) \\
p_p^2c^2 &= T_p(T_p+2mc^2);
\end{aligned} \tag{2.15}$$

where α and β are the angles made by electron and positron with the original track of the photon. If the minimum possible kinetic energy of electron and positron is taken to be 0, then the minimum energy of photon to produce the electron-positron pair is the sum of the rest mass energies of the electron and positron. Thus the minimum energy required for pair production is

$$\hbar\omega_{min} = 2mc^2 = 1.022\,\text{MeV} \tag{2.16}$$

Thus, we can expect pair-production only by high energy particles. Also, in the above equations Eq. 2.15 it is seen that the equations are not simultaneously solvable. To balance the momentum there has to be another particle. Thus pair-production can not occur in absence of any medium.

Cross-Section of Pair-Production

The cross-section of pair production is given by [11]

$$\frac{d\sigma_{pair}}{du} = \frac{2\alpha^2 r_e^2}{3\pi} Z^2 \frac{1-u}{u} \int \left[F_e(r) + \frac{m_e^2}{m_\mu^2} F_\mu(r) \right] dr; \tag{2.17}$$

where $r = (E_{e^+} - E_{e^-})/u$ and F_e and F_μ are complex functions of r, u and Z.

2.2.4 Photoproduction

As suggested by the name, photoproduction is a process of emission of a virtual photon. In contrast to the virtual photon emitted in pair-production, the photon produced interacts hadronically with matter and generates secondary hadrons. Since the production of a pion (a hadron) requires a center mass of energy at least equal to the sum the proton and pion masses, only high energy virtual photons are important and the cross-section at muon energies on the order of GeV is very small.

Cross-Section of Photoproduction

The cross section of photoproduction is given by [11]

$$\frac{d\sigma_{ph}(E_\mu)}{du} = \frac{A\alpha}{2\pi} \sigma_{\gamma N}(uE_\mu) u \times F\left[E_\mu, u, \sigma(uE_\mu)\right]; \tag{2.18}$$

where u is the usual fractional loss of energy of muon and $\sigma_{\gamma N}$ is the interaction cross-section of real photons with the nucleons. The function F is decided by mass hadrons and u.

2.2.5 Relative Magnitude Energy Loss-Processes of Muon

For low energy (MeV) muons the energy loss of due to ionization is dominant. Bethe-Bloch Eq. 2.5 nicely describes the behavior of energy loss of muon. For higher energy (GeV) of muons the radiative energy loss process dominates the ionization.

Figure 2.2 depicts how the stopping power of muon due to different process changes as the muon energy goes from MeV to TeV.

In the radiative process of muon the cross-section of pair-production dominates the bremsstrahlung. It is seen, the cross section of pair-production is proportional to $\alpha^2 = (1/137)^2$ whereas the that of bremsstrahlung is proportional to $\alpha = (1/137)$. It is usual to expect that the cross section of bremsstrahlung is higher. However, the term $(m_e/m_\mu)^2$ present in the bremsstrahlung cross-section formula plays an important role in making it smaller than the cross-section of pair-production. Photoproduction cross section is very low in comparison to that of other two radiative processes. The picture 2.2 shows the relative magnitudes of differnet mechanisms of energy loss of muons.

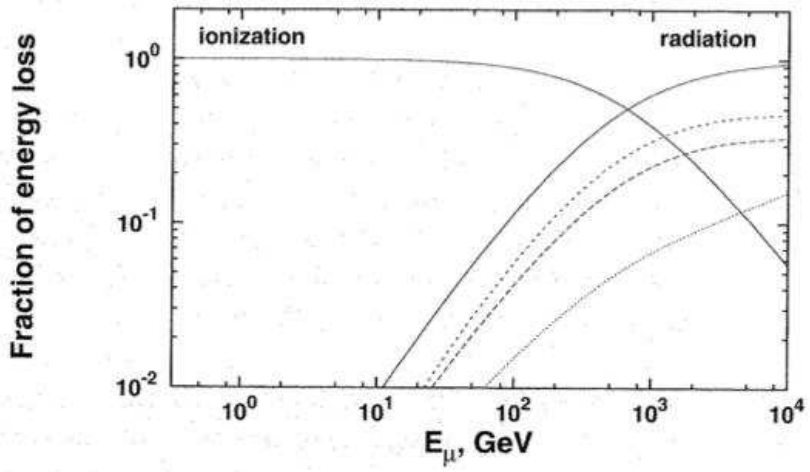

Figure 2.2: Fraction of loss of energy through different radiation processes as a function of the muon energy normalized to the total energy loss per g/cm^2. The short-dashed curve is for pair-production, the long-dashed curve for bremsstrahlung, and the curve below the bremsstrahlung curve for photoproduction [11].

Chapter 3

The Detectors

The MINOS experiment consists of three detectors: the Far Detector, Near Detector and Calibration Detector. The Near Detector is located at Fermilab in Batavia, Illinois, USA. It is situated immediately after the NuMI neutrino beam. The Far Detector is situated 732 km North-East from Fermilab in the Soudan Underground mine in Tower, Minnesota, USA. The Calibration Detector resided at CERN in Geneva, Switzerland, until its dismantling in January 2004. Although all the detectors are intrinsically similar in their detection of particles, to minimize potential systematic differences, the Calibration, Near and Far Detectors' purposes are subtly different, along with their construction. The primary purpose of MINOS is the detection of neutrinos from distant beam. The Far Detector was made as large as possible to be able to examine events from a neutrino beam that widens from tens of centimeters at the beam source (right before the Near Detector) to a diameter of a few kilometers by the time it reaches the Soudan mine. The Near Detector is outfitted very similarly to the Far Detector, but the electronics are adjusted to compensate for a significantly higher flux of events than that of the Far Detector. The Calibration Detector used components from both the Near and Far Detectors to evaluate the different responsiveness of the Far and Near Detector electronics and setup under the same conditions.

Although the MINOS detectors are primarily built for the detection of neutrinos, they are equally responsive to cosmic ray muons. The Far Detector is on the 27^{th} level of the former U. S. Steel Corporation Iron Mine at the depth of 713 m below the surface. The significant features of the location are a sufficient distance from the neutrino source and a sufficient depth to provide shielding from the terrestrial and cosmic radiation. The Far Detector receives only high energy ($>100\,\mathrm{GeV}$) muons because most of the low energy muons are

filtered by the rocks on the path. This is the reason why the Far Detector is preferred for the study of high energy muons. The major sub-systems of the detector are: steel, active scintillator, magnet and electronics. A neutrino enters the detector where it interacts with the steel and produces a charged particle. This daughter particle then enters the scintillator module and produces photons. These photons are transmitted via a fiber optic cable to a photomultiplier tube (PMT), which turns the small light signal into an electrical signal that is recorded by the Data Acquisition System (DAQ).

3.1 Steel

The detector is composed of octagonal identical 486 steel planes of thickness 2.54 cm and approximate diameter 8 m . The total weight of the planes is 5.4 kt. The planes are placed parallelly separating each other by 5.94 cm. The gaps utilized to place scintillator strips. Also, the gap provides ample space for air flow keeping the detector cool. The center of each planes has a bores of 30 cm radius. A Magnetic coil passes through the coil providing magnetic field to the detector. The steel planes are oriented in such a way that horizontal NuMI beam hits perpendicularly to the face of each plane. The steel planes are arranged in two distinct groups, called supermodules (SM), with a gap of 1.5 m separating SM1 from SM2. The space between supermodules allows for the installation of the magnetic coils.

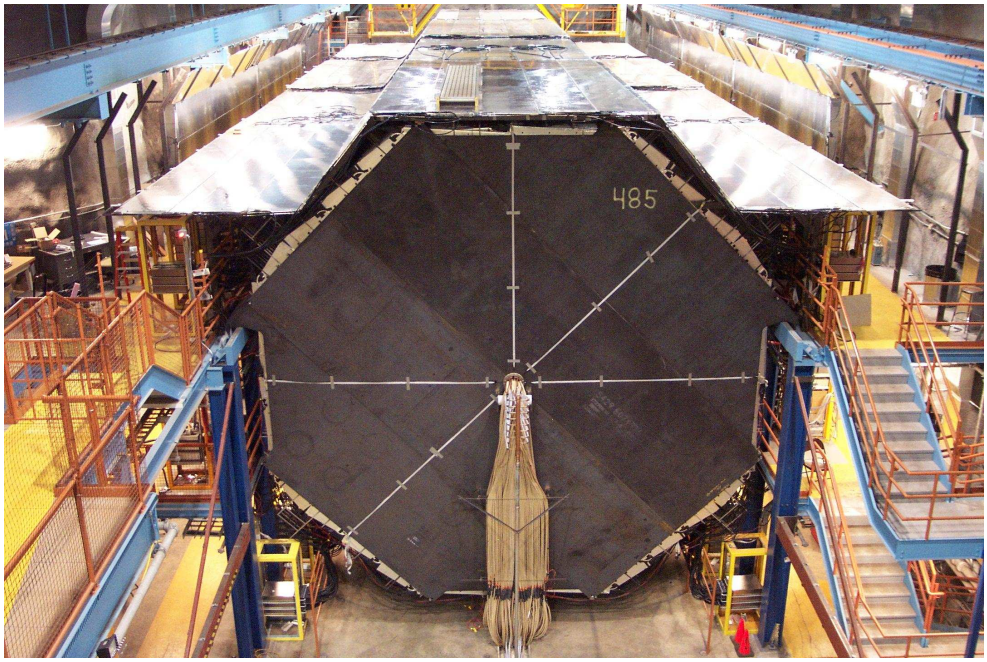

Figure 3.1: The front view of the far detector, showing the octagonal plane structure , the veto shield on the top , the magnet coils coming out of the center of plane, and the electronics rack on side of the detector planes.

While the steel is largely unnecessary for the detection of cosmic ray muons, the detection of a neutrino and the structural integrity of the scintillator modules depends on it. Exacting alignment of the planes is necessary in a precision particle physics experiment, and the steel insures that the scintillator modules will not shift or sag in the course of their duty. A ferromagnetic material is required to produce a strong magnetic field that will bend the path of a charged particle to allow charge sign determination. The steel is an integral component of this magnetized detector, unique in its ability to determine the charge sign of sampled particles [1].

Structurally the Near Detector is slightly different than the Far Detector in shape and size. There are 282 steel planes of total weight 0.98 kt. It is situated at the end of NuMI beam facility at Fermilab in a 100 m deep underground cavern.

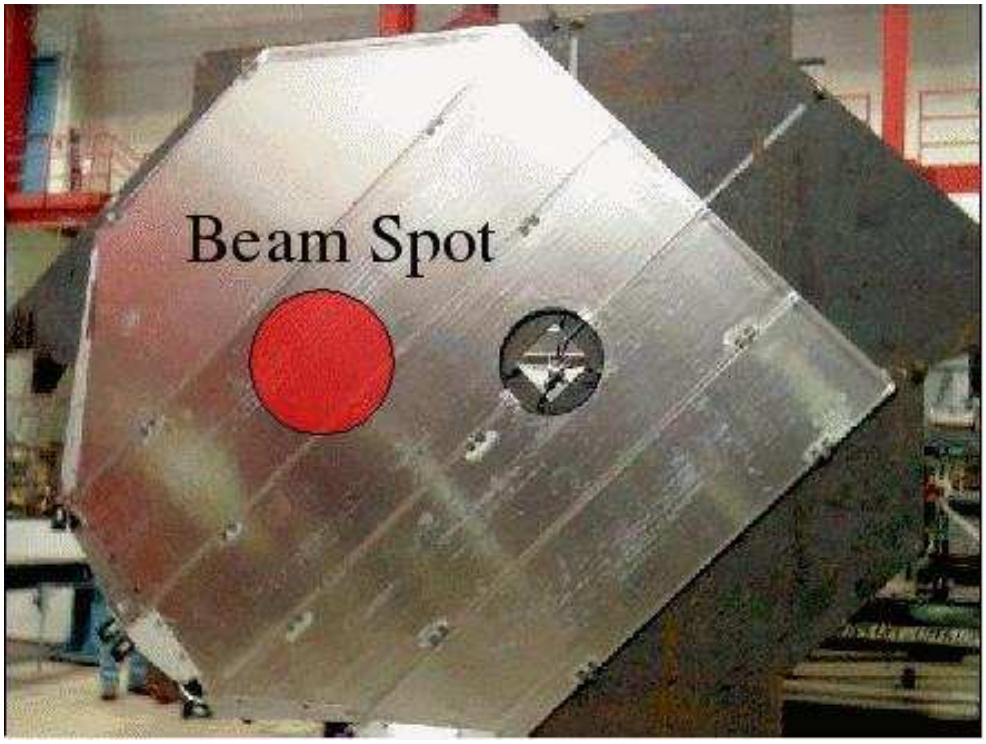

Figure 3.2: The Near Detector with a superimposition of the beam cross-section. The hole in the middle is for the magnet, which is 50 cm offset from the beam.

3.2 Active Scintillator

The active detector component is the scintillator, strips of extruded polystyrene 1 cm thick and 4.1 cm wide. The polystyrene is enhanced with the fluors PPO (1%) and POPOP(0.030%). These strips are formed with a center groove to hold the wavelength-shifting (WLS) fiber and are co-extruded with an outer layer of TiO_2 for internal reflectivity [13].

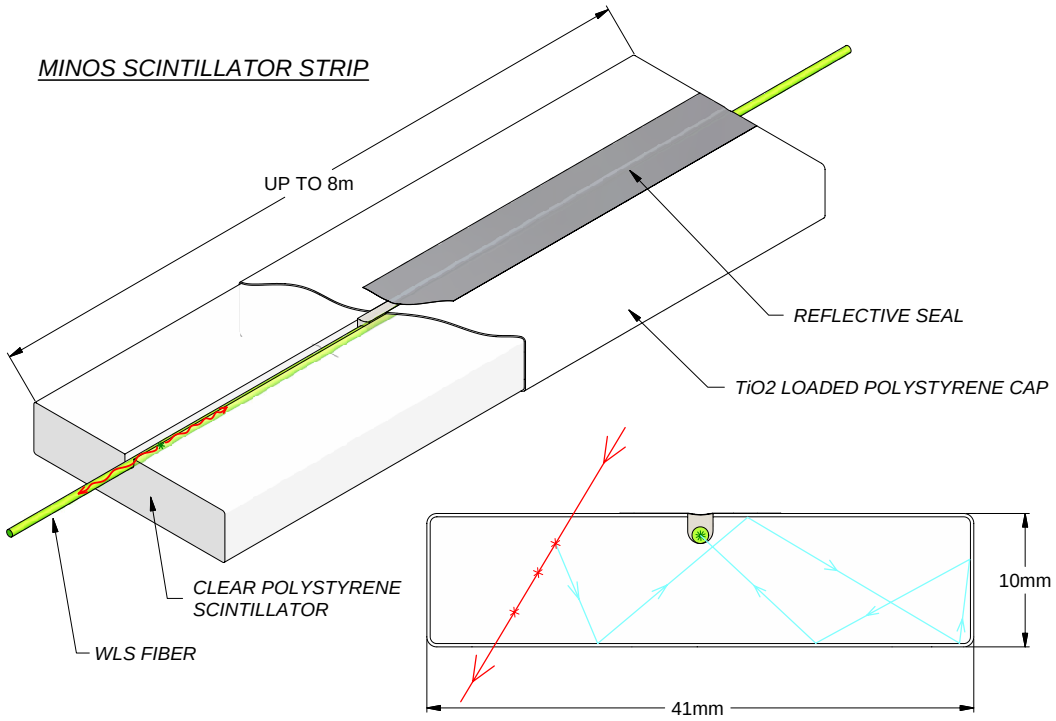

Figure 3.3: Cutaway drawing of a scintillator strip. Ionizing particles produce light inside the strip. The light is multiply reflected inside the strip by the coating of the strip. The light is finally absorbed by WLS fibers [14].

Panels of either 20 or 28 strips are joined to make an array of 192 strips for each octagonal detector plane. The modules are produced in a number of distinct groups for ease of fabrication and detector readout.

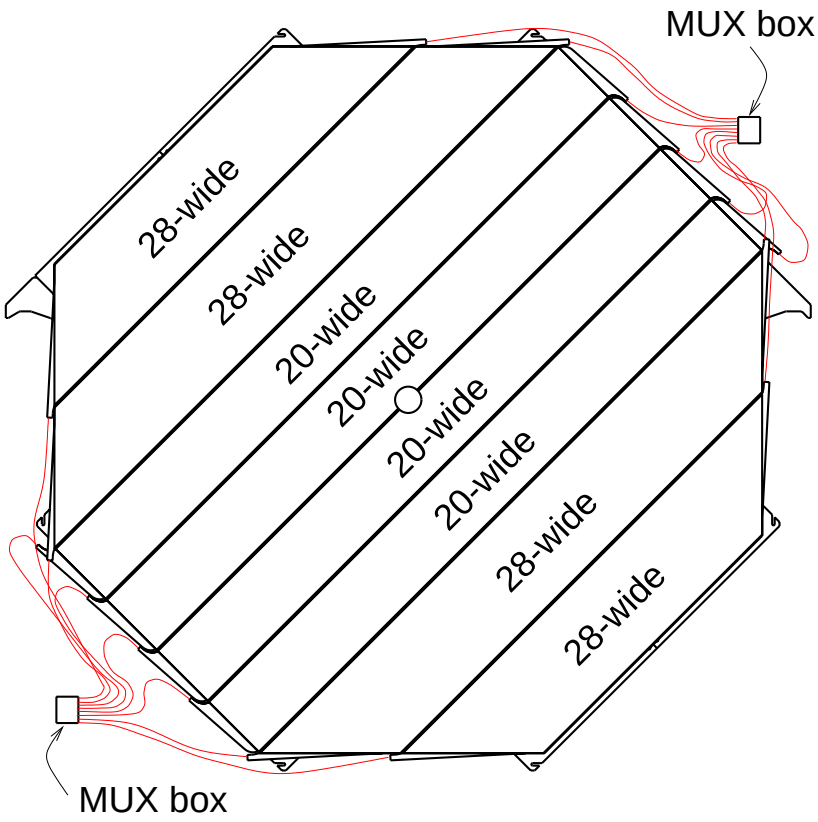

Figure 3.4: A schematic showing the module layout as well as the connections to the MUX boxes, the front end electronics component that contains the PMT assembly [1].

As a charged particle traverses the detector modules, it deposits energy in both the steel and the scintillator. The energy that is deposited in the scintillator is re-emitted in the form of UV photons. These photons are internally reflected off the walls of the strip until some of the photons are absorbed by the WLS Y-11 fluor that traverses the strip. The absorption spectrum of the WLS Y-11 is centered on 420 nm (violet), and only overlaps slightly with its emission spectrum centered beyond 470 nm, in the green band of visible light. Shifting the wavelength of the incident light is an effective method to minimize self absorption. The WLS fibers end at the terminus of the scintillator module, where they connect to an array of clear optical fibers to complete the path of the photons from the scintillant to the PMT.

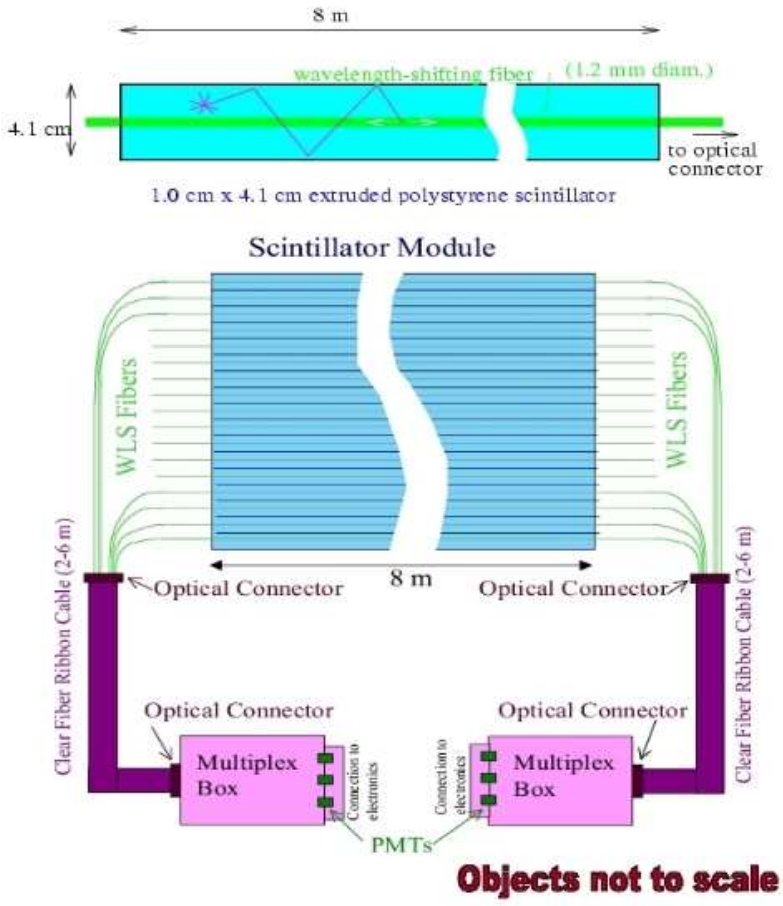

Figure 3.5: A drawing showing the module design and scintillator layout [1].

The planes of the detector are organized in a rectangular coordinate system, nominally referred to as U and V. The strips on each plane are arranged at an angle of 45° with the horizontal, the U planes a 90° rotation from the V planes. The choice of (U,V) facilitates connections to both ends of the scintillator strips. This provides a set of mutually orthogonal coordinates with which to measure a particle's location in the detector. The orientation of the orthogonal axis can be seen in figure 3.6 on the next page.

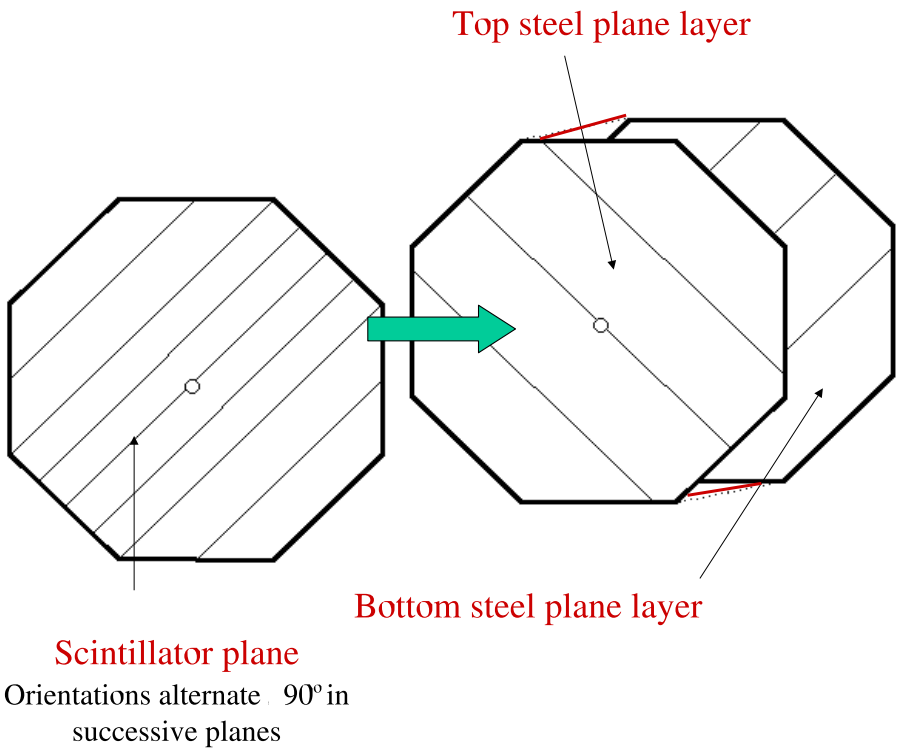

Figure 3.6: The relative orientation of U and V planes [15].

"Vertical" and "horizontal" positions are determined by a particle hit in a combination of two or more planes, at least one U and one V, and depth is found by simply counting how many planes the particle traversed.

There are a number of electronics subsystems that the light signal encounters after traveling to the PMT via the WLS fiber. The first step in the electronic journey is the encounter with the PMT that converts light to an electrical signal via the photoelectric effect. The process of converting light into electricity makes a PMT "basically an inverse light bulb" [15]. The photon is absorbed in the PMT by a photoemissive cathode, where the photon excites the material, which then emits electrons. These first few electrons are accelerated with a large electric potential toward a dynode, where more electrons are created. These electrons are again accelerated in the same manner, and the cascading effect continues until the now amplified signal reaches the anode of the PMT, where the signal is then ready to be used.

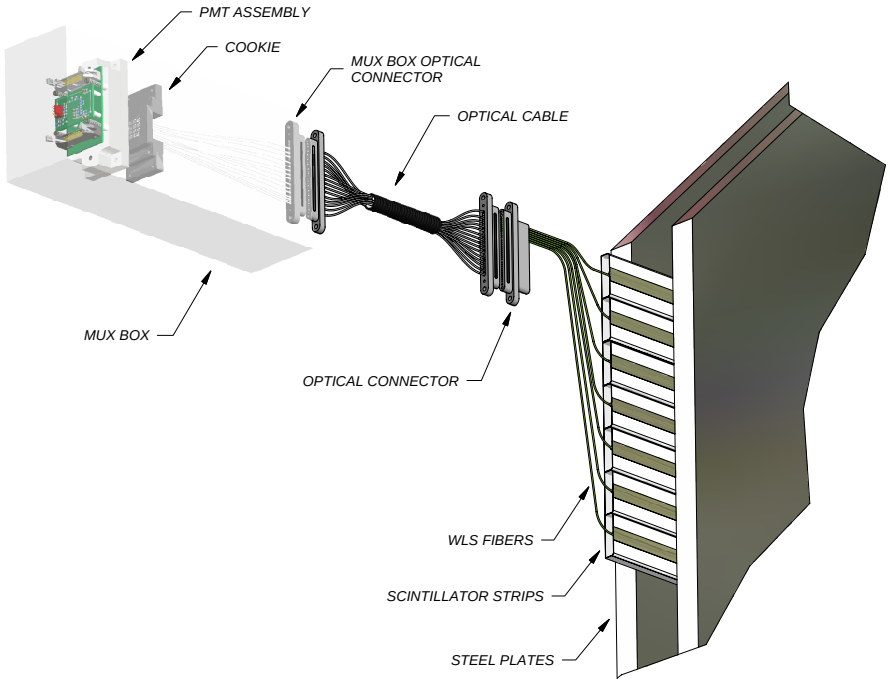

Figure 3.7: Cut-away of the connection of the PMT to a module. The light produced in the strip 3.3 travels out of the module in a WLS fiber, and is then carried by a clear optical fiber to a MUX box where it is routed to a pixel of the PMT assembly [14].

3.3 Magnetic Field

MINOS is the first neutrino experiment able to discriminate neutrinos from antineutrinos, and this capacity is derived from the magnetic field. The Far Detector has a toroidal magnetic field produced by a 15,000 A-turns current, generated by an 80 A current run through 192 turns of stranded copper wire housed inside a 25 cm diameter, water-cooled, copper jacket, formed into a coil running the length of each supermodule. The average magnitude of the magnetic field is 1.5 T at a radius of 2 m [16]. The magnetic field began operation in a nominal "field forward" direction to focus μ^-, thus increasing the detector acceptance.,The current can easily be reversed for the reverse polarity of the field. This is a vital capability that allows the study of detector spatial irregularities and slight magnetic field asymmetries. Data can be taken with a particular field configuration and compared with reversed field data, with the ideal case resulting in particle

tracks with a mirror image of the tracks from the original. Once the detector is well understood, this will provide an important cross check for charge determination efficiency. The desired neutrino signal is detected as charged particles interacting with the detector components, while the neutrino is itself a neutral particle. The beauty of using a magnetized detector for such studies is that interaction of an energetic charged particle with a magnetic field is well understood, so the direction of curvature of the particle's motion compared to the direction of the magnetic field allows a determination of charge sign, while the radius of curvature is used to deduce momentum. This illustrates the pioneering status of MINOS as the first deep underground detector to be able to separate μ^+ from μ^- directly, and by extension, ν_μ from $\bar{\nu}_\mu$.

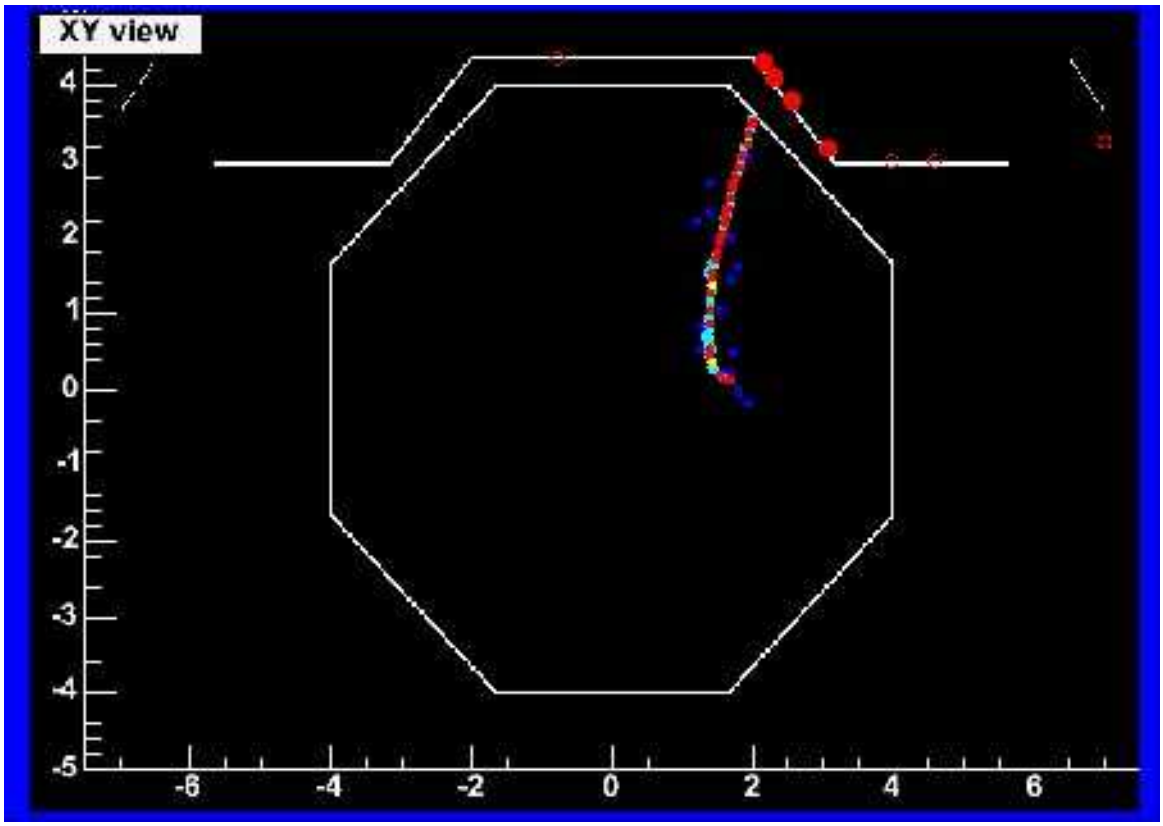

Figure 3.8: The effect of the magnetic field on a charged particle inside of the detector. In the face-on view of the detector the colored curve is the track of muon. Because of magnetic field the direction of charged particle bends making a curved track. Signature of entrance of cosmic particles is seen on the veto shield (on right top corner). The single track indicates a particle entering the detector. The curvature of the track is small in the beginning. As a result of lose its energy through ionization (there is no shower in current event display) the curvature is continuously increasing [15].

The distribution and strength of magnetic field in the Near and Far Detector are slightly different. The near detector coil hole is offset 55.8 cm from the center of the plane and the detector is placed so that beam is centered halfway between the hole and the left vertical edge of the plane as shown in figure 3.9. Because of squashed-octagon geometry, a 40 kA-turn current is required to achieve sufficient field.

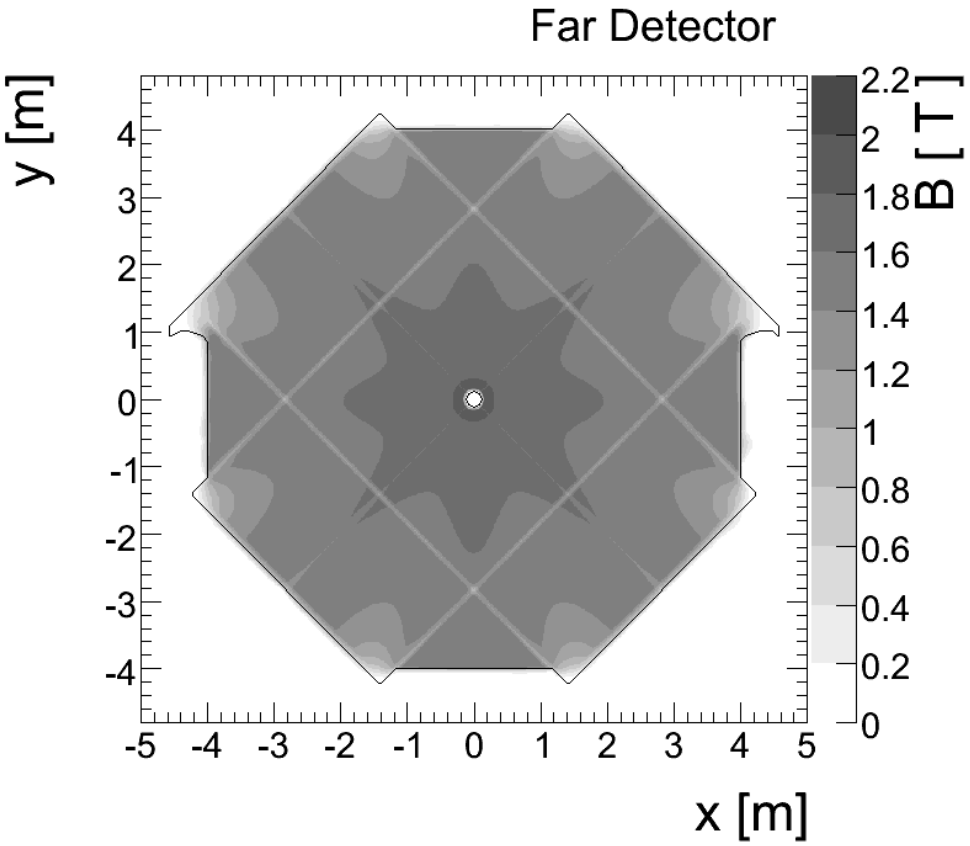

Figure 3.9: Magnetic Field maps for far detector plane. The gray scale indicates strength of magnetic field B [14].

3.4 Calibration

To make sure that the WLS fibers and electronics of the Detectors are working properly a few Calibration checks have been constructed. The two main quick calibration tools that are used are the Light Injection (LI) system and the Charge Injection system. As the response of the detector changes, because of changed electronics, drifting voltages for electronics, power surges that may fry some electrical connections etc. These tools are used to either identify problems or to monitor short timescale drifts of Detector response.

The method behind the LI system is to inject a known amount of light light onto the WLS fibers, monitor

the output and then calibrate the response. Light from an ultra-violet LED illuminates 70 fibers in a pulser box. Groups of these LI fibers are then strung to light injection manifolds that are attached to the ends of the scintillator modules. The light injection mimics an event in the detector, but since the input pulse height of the light can be controlled, it is possible to compare the input of light to the output signal. The response of the electronics and PMT to a linearly increasing pulse height of light from Pulser box is itself linearized and that way data can be verified as having a well known conversion from pulse height to charge. The input light is also independently monitored by two PIN diodes to make sure that the input signal is outputting the correct signal.

Charge injection is similar to the LI system except that it bypasses all the optical fiber and the PMT. The charge injection mimics a signal from the PMT and is used to linearize the Analog to Digital Conversion (ADC) scale. This method is used to isolate problems that may occur when the PMT and fibers are functioning correctly, but the electronics are not working properly. It is also essential in linearizing the response of the PIN diode electronics used in the light injection system.

3.5 Veto-Shield

In order to reduce the background in the measurement of atmospheric neutrinos arising from the cosmic rays entering the top sides of the Far Detector, a veto shield covering these areas are installed. The veto shield is constructed with the same scintillator material used in the detector, and differs from the detector planes only in its orientation and the fact that it does use not have same steel backbone. The veto shield lies perpendicular to the detector planes, and uses their stability for support. Not only the design of the veto shield eliminates the cosmic ray events from the set of beam neutrino data, it also adds purity cut for the scientific study of cosmic rays. Any muon that passes through the veto shield will enter the detector through the smallest amount of rock overburden; these are the lowest energy muons the Far Detector accepts.

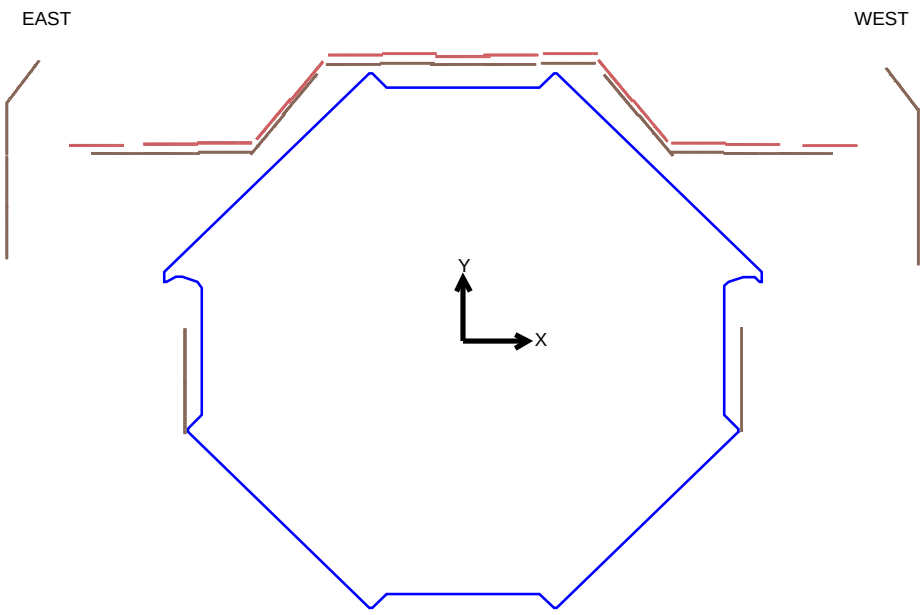

Figure 3.10: Schematic of the components of the veto shield. Both scintillator modules that comprises the shield are shown, including the double layer above the detector. Figure 3.8 shows how the veto shield keeps record of incoming particle before it goes to the detector [1].

Chapter 4

Data Analysis

The analysis and interpretation of data obtained from the detector is as equally difficult an issue as the collection of the data. In the case of MINOS particle data analysis, the difficulty lies in identifying the particle, understanding how the particular particle interacts with the detector, and understanding the physical processes that give rise to the class of particles. In the present analysis I have included three steps: Analyze Monte Carlo simulated data to decide different cuts; compare the Monte Carlo simulated data with the real data collected from the detector; and decide the cuts required for the detector data to select events showing the radiative energy loss.

4.1 Monte Carlo Simulation

In computational science the term "Monte Carlo" is the class of algorithms that rely on repeated random sampling to compute the result. So, it is a statistical (based on probability) method of finding the result of some phenomena. One might reasonably ask whether the study of science can be aided by such probabilistic interpretations, but in fact, with Monte Carlo techniques, very complicated scientific and mathematical problems can be solved with considerable ease and precision [17].

From theoretical investigations on the behavior of elementary particles and from past analysis of cosmic ray data, we have accumulated a hand full of information about cosmic rays, muon production, muon interaction with materials, particle energy deposition in scintillator, and PMT response to deposited energy. This information can be applied to simulate expected detector response. Simply applying analytic mathematics to

detector components does not adequately simulate the physics of the particle detection that happens on an event by event basis. Rather, the input is generated at random from known probability distribution, subject to physical processes [1]. This process is called *Monte Carlo* (MC) method and the data produced through this method are called "MC data".

4.1.1 Structure of MC Data and Tolls of Analysis

The MINOS cosmic ray MC data contains a wealth of information such as: where a particular particle enters and exits; the angle through which the particle enters the detector; how much energy does a particle lose in each strip of the detector etc. In the data all we have is the histogram of corresponding variable. The object oriented computational language ROOT, based on the popular computational language C^{++} is used to analyze the histograms [18] [19]. As a first step of analysis, using advanced computation techniques and calibrations of the required variables, an "Ntuple" is prepared. The Ntuple stores data of the basic data types in an easy to access format in which data variables can be manipulated, plotted and fitted. The Ntuples are produced during production running as an end product of the standard reconstruction (the process of interpreting physical meaning from a collection of light in the detector) are called Standard Ntuples. Each Standard Ntuple file contains one or more Ntuples, each in the form of a ROOT TTree.

The Standard Ntuple has a lot of information. Selection of the right variables for the study of interest is the first task. For example, in the current analysis, information about tracks made by the particles in the Detector, electromagnetic showers produced in the Detector due to interaction of the particle with the material of the Detector and orientation of the track are the most important. As a tool to analyse the data, the computer programming language C^{++} is extensively used. The object oriented programming language CERN's ROOT V5.22/00b [http://root.cern.ch] is used create graphs and histograms. MINOS' customized version of ROOT, LOON is also used.

4.2 Structure of Detector Data

The original structure of the Detector data are in binary format. The data in such format are calibrated and re-written in the Ntuple. The structure of the Ntuple of the Detector data is similar to the Ntuple of MC data. So, the analysis technique applied in the MC data fits for the Detector data as well. However there are two issues to take care while while using the Detector data. One is reliability of calibration of some of the data.

The error associated with some of the variables is very large for some ranges of magnitudes of the variables. We can not rely on such data. For example, the momentum of magnitude greater than 100 Gev/c associates very large error. The other issue is size of the Ntuple. As the name suggests, Standard Ntuple has a lot of variables. Such a bulky Ntuple data occupies a lot of space to store. Also, such bulky file consumes a lot of processing time when analyzing it on the computer.

Throughout the current work, I have used the NONAP Ntuple (NoNtuple) for the analysis of Detector data. The NoNtple is almost similar in structure of Standard Ntutuple but it contains only selected and required variables for the present analysis. A small size and user friendly names of the variables are its interesting features. Exploiting the flexibility of adding variables, I added some of the variables required for my analysis. Some of the important variables I added are meuSD (deviation of total PH from MEU), EastAverage (average of PH at East side of strips), WestAverage (average of PH at West side of strips) etc. The picture below shows a snap of included variables.

The most of the credit for preparation of NONtple goes to Jeff De Jong. During its preparation I made contribution in adding variables suitable for the cosmic muons analysis. The compilation on NoNtple codes produces the NoNtuple data. But the compilation itself takes very long CPU time (the amount of time for which a central processing unit (CPU) is used for processing). To accomplish such a task a CPU would take months to create NoNtple data of one year. However, using many CPUs at the same time we reduced the time. For this task special specialized computing package “Condor”. Condor is a specialized workload management system for compute-intensive jobs. Condor provides a job queueing mechanism, scheduling policy, priority scheme, resource monitoring, and resource management. Users submit their serial or parallel jobs to Condor, Condor places them into a queue, chooses when and where to run the jobs based upon a policy, carefully monitors their progress, and ultimately informs the user upon completion [http://www.cs.wisc.edu/condor]. I made significant contribution during compiling the NoNtple code in the MINOS Condor.

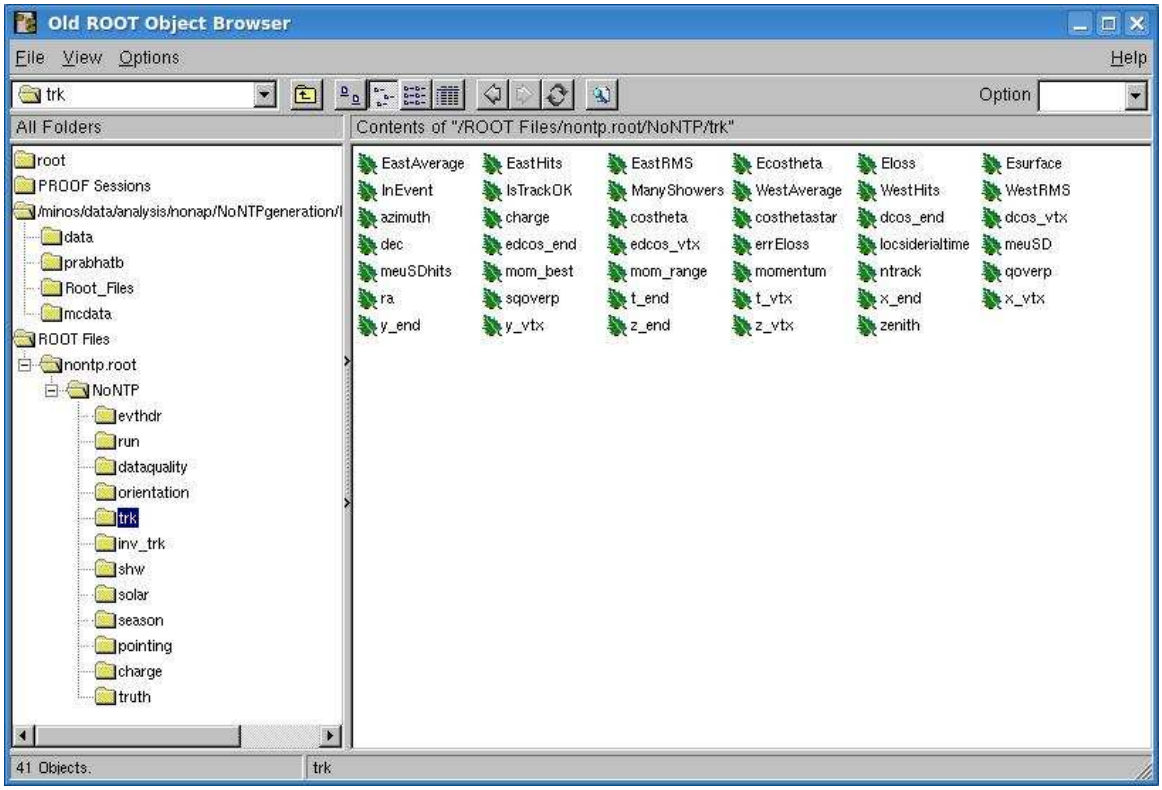

Figure 4.1: A snapshot of display of entries in a branch (track header) of NoNtple.

4.3 Selection Cuts

All the data obtained from the Detector does not carry physical meaning. Even if the data carry physical meaning, they may not be interesting for all analysis. So, to select the events bearing physical meaning and lying in the region on interest several cuts are to be applied to remove the unwanted events. The process of elimination of unwanted events from the collections of events is referred as a “cut”.

There are two important points to account while applying the cuts. One is the purity of the output. After filtering out the uninteresting events from the total events, a handful of required set of events is obtained. But in the output there still may present unwanted events. The fewer the number of unwanted events in filtered sample, the higher is the purity of the output. This computing algorithm is the tool for filtering events. Thus, purity of a particular algorithm is :

$$Purity = \frac{Number\ of\ good\ events\ in\ selected\ set}{Total\ number\ of\ events\ in\ selected\ set}$$

For example, if a selected set of 100,000 events contains 30,000 high energy events then the *purity* is 30%

The other point is the efficiency. To meet the objective of creating pure sample, a lot of unwanted events are thrown out. But, together with the unwanted thrown events a lot of good events may also be sacrificed. The lesser the number of thrown away good events, the higher is the efficiency of algorithm.

$$Efficiency = \frac{Number\ of\ good\ events\ in\ selected\ set}{Total\ number\ of\ good\ events\ in\ entire\ sample}$$

For example, if we start with 100,000 high energy muons before algorithm and after all the cuts there are 40,000 left, then the *efficiency* is 40% While writing any such filtering algorithm, higher value of both purity and efficiency are expected. However, as a general rule of nature, the increase in one leads to decrease in other. Thus, my goal is to search for the algorithm to optimize both purity and efficiency. For the cuts, the product $purity \times efficiency$ is maximized.

In the current work, to select the events with high energy, I have applied several cuts.

a. Basic Cuts

► Shower

It is assumed that all the high energy muons lose their energy through radiative processes (see Ch. 2). It is reasonable to assume that the muons produce electromagnetic shower in the detector during the loss of energy through radiative processes. So, tracks of muons having no shower are removed. To illustrate the meaning of shower, two events with and without shower in track are shown.

The graph below shows the distribution of showers. There handful of events without shower. The number of showers produced in an event even goes up to 9.

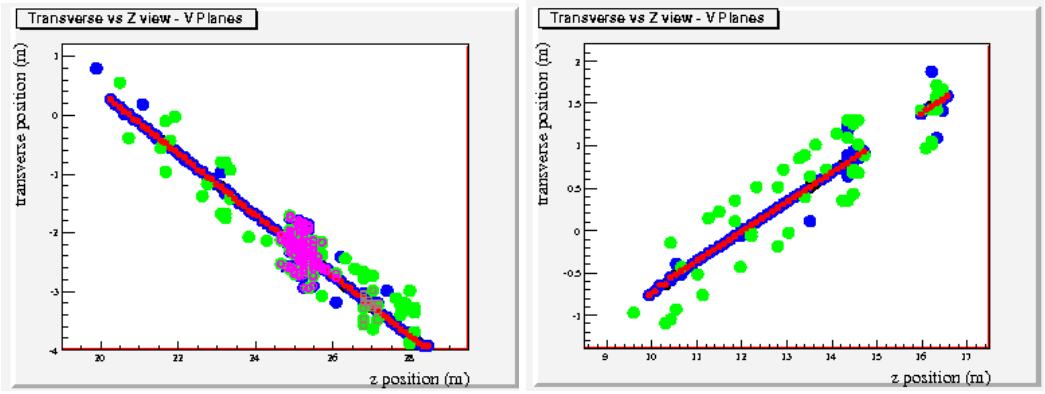

(a) Showering Event (b) Non-Showering Event

Figure 4.2: An Event Display of a typical track of muon. (a) The track has two showers, one of which is prominent. The shower is indicated by chunk of pink color. The larger chunk of color indicates the larger loss of energy of the muons. (b) The track has no shower; it is losing energy only by ionization.

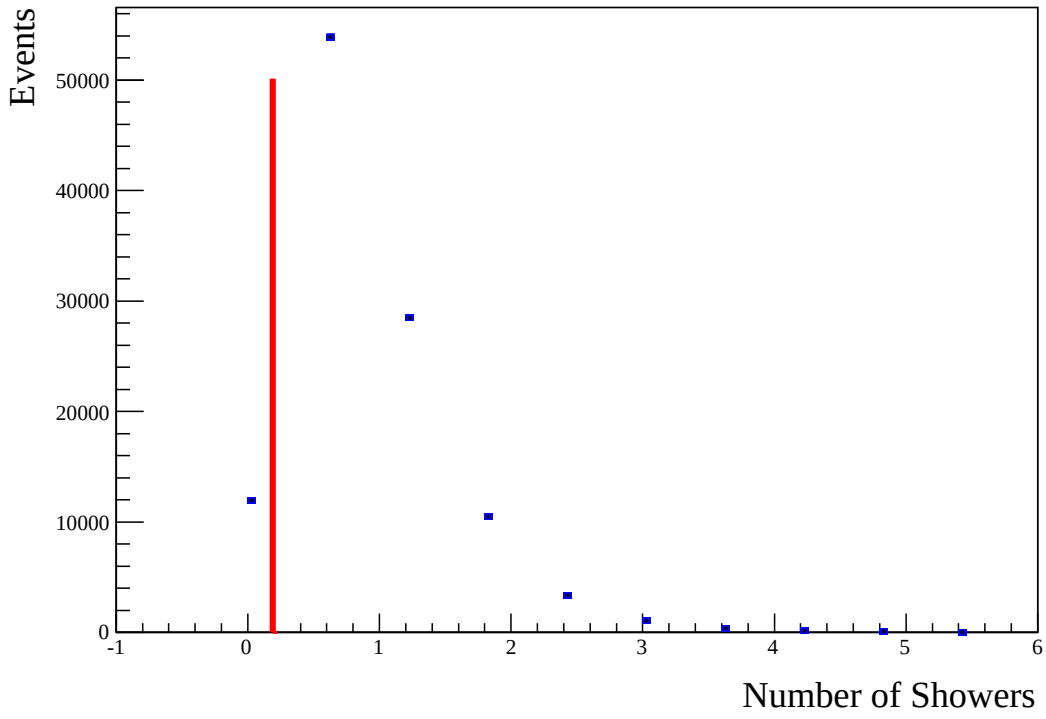

Figure 4.3: The number of showers produced in the track. The red vertical line indicates the place where the cut is applied. All the events to the left of the red line are cut. The small error bars are statistical.

► Curvature

Because muons are a charged particle, their paths are curved in presence of the magnetic field of the Detector. The angle of deviation from the original path depends upon the energy of incoming muon. The larger the energy of muon, the smaller is the angle of deviation. From the available information of the detector, it is hard to find the exact radius of curvature of the track. Without loss of generality, the curvature can be redefined as:

$$\cos(curvature) = (track\ vertex) \cdot (track\ end);$$

$$curvature = \cos^{-1}[(track\ vertex) \cdot (track\ end)] \times 180^{\circ}/\pi;$$

where *track vertex* and *track end* are the unit vector of muon track at vertex and end of the track.The " $\cdot$ " indicates the vector dot product between them. So the curvature is the angle of deviation of the muon track measured in "degree". To select high energy events all the tracks with curvature larger than 1° are are removed. Using the physics of bending of the charged muon in magnetic field of the Detector the curvature of 1° corresponds the energy of about 200 GeV.

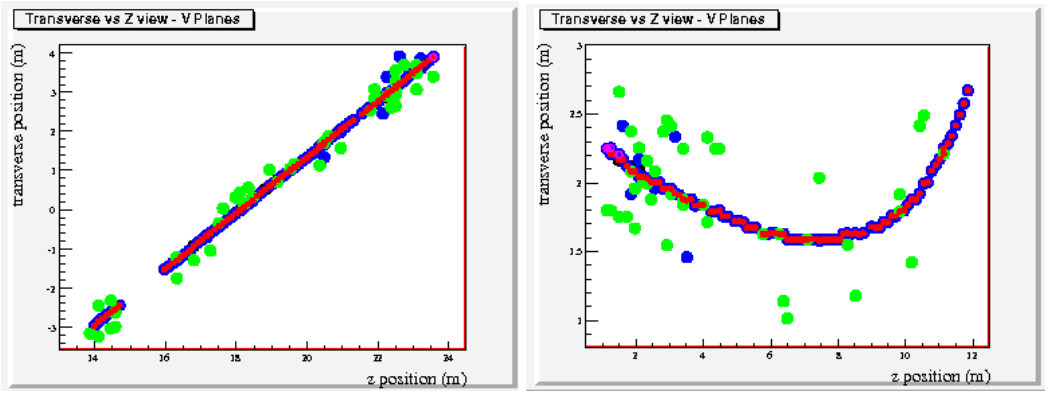

(a) Small Curvature (b) Large Curvature

Figure 4.4: An Event Display of a typical track of muon. (a) The curvature of the track is small, almost 0, and (b) the curvature is large, more than 10°. The smaller curvature indicates the larger energy of the muons.

The figure below shows the distribution curvature of track of MC data. The majority of the curvature are less that 1. However the curvature of some events goes even above 10 degrees.

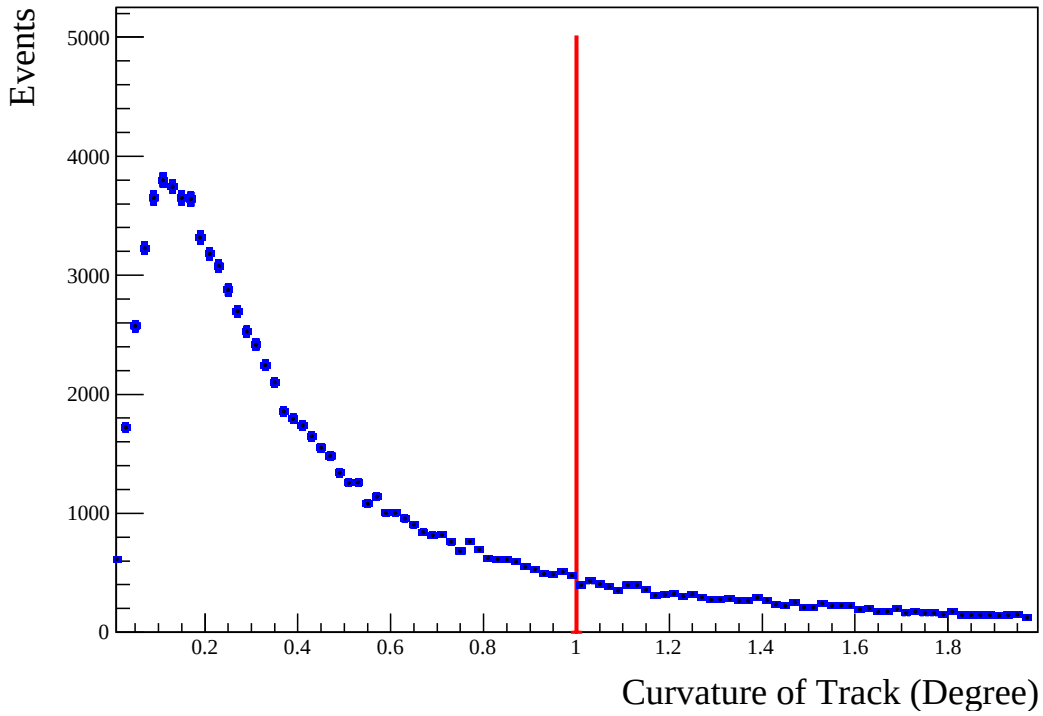

Figure 4.5: The distribution of curvature of the track. All the events those lie right to the vertical red line are cut. The error indicated is statistical error. The error bars are small enough to see distinctly.

► Fiducial

Only the information of the track within the fiducial volume of detector is is reasonable for the analysis. There are some events whose vertex and/or end lies outside the fiducial volume. Such data are discarded for analysis. The detector is approximately a cylinder of diameter 8 m and length 30 m. So, all the events whose vertex and/or end is at distance greater than 4.5 m from the center of the cylindrical axis are removed.

The distribution of the length of the distance of track vertex from the center of the plane of the Detector. It is seen that there are a number of events having the length more than 4.5 m.

► Track Length

Length of track of muons in the Detector is related to the energy carried by the muons. Muons with higher energy penetrate the detector while the muons with lower energy are stopped within the detector. For the best

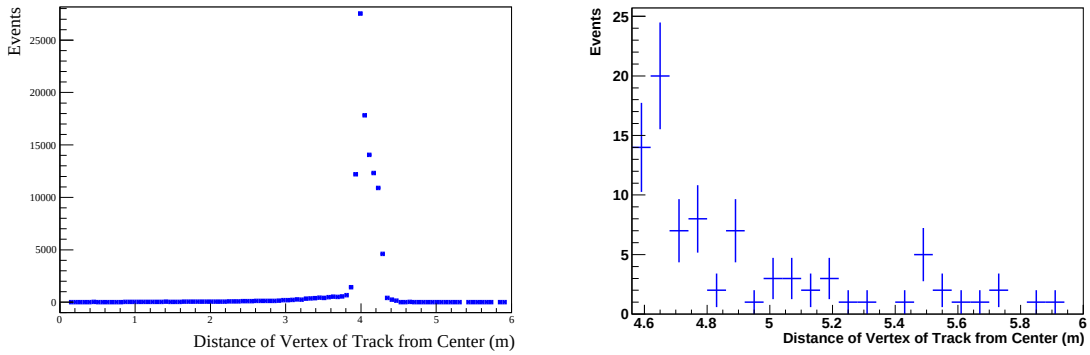

(a) (b)

Figure 4.6: The distribution of the distance of vertex of the track from the center of the Detector plane. The error bars indicate the statistical error. (a) Over all distribution of the distance and (b) the distribution of length more than 4.5 m.

efficiency and purity all the events having track length shorter than 10 m are considered as low energy events and are removed. Using approximation of energy loss of muons in matter, threshold energy of muons to cross the length of 10 m comes to be about 7 GeV. Also the events which penetrate less than 2 m of axial length (z-length) are removed

The Fig. 4.7 shows the distribution of the length of track for MC data. It is seen that the distribution is smooth above the length of 10 m.

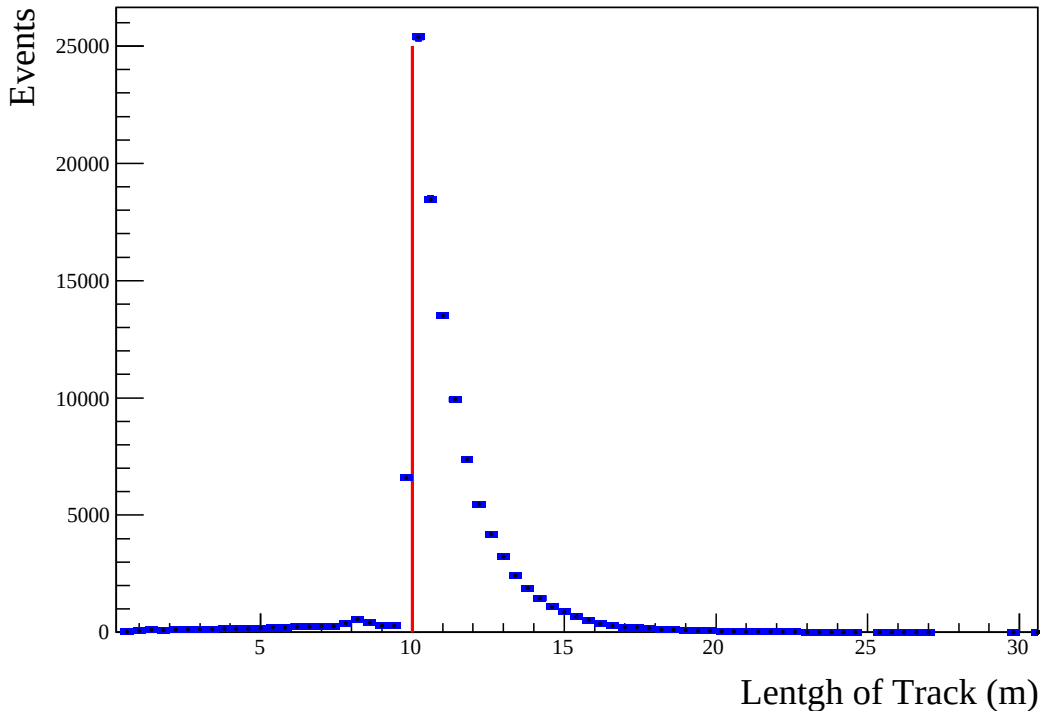

Figure 4.7: The distribution of the length of the tracks. All the events whose length lies left of the red vertical line are cut. The error indicated is statistical error. The error bars are small enough to see distinctly.

► Plane

In the analysis we encounter with some events in which the could interact within only few planes. Even if such events could be high energy events, the information obtained from few planes is statistically less reliable. So, the events those cross fewer than 20 planes are removed.

The Fig. 4.8 shows the distribution of the number of planes crossed by the muon tracks.

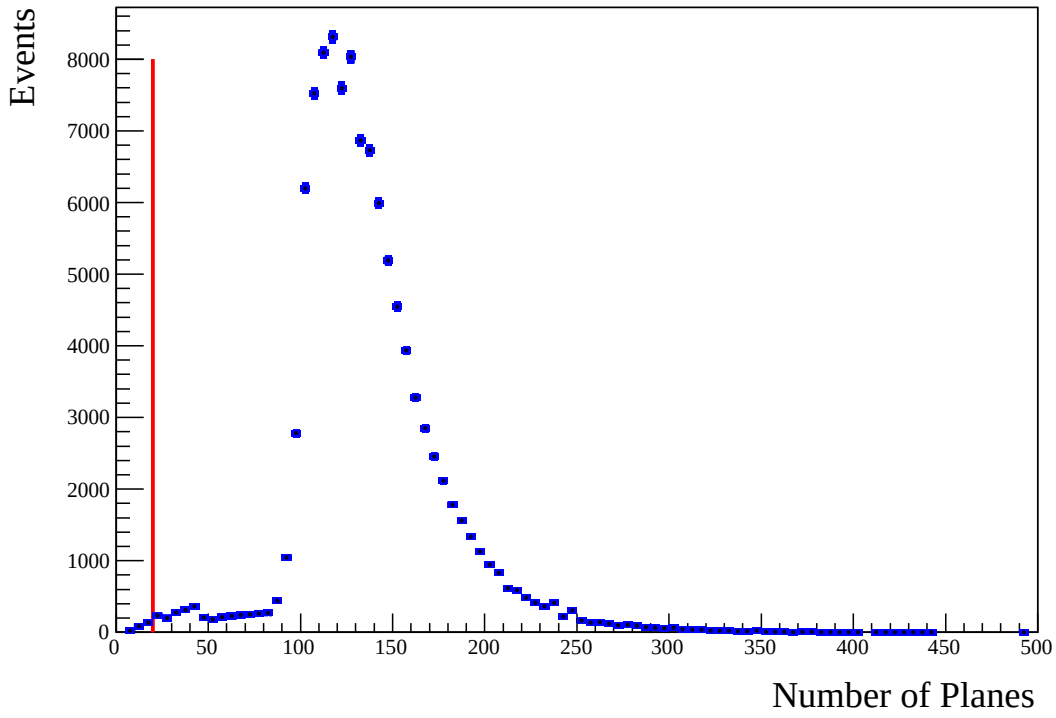

Figure 4.8: The distribution of number of plane crossed by a track. All the events lying left of the red vertical line are cut.The error indicated is statistical error. The error bars are small enough to see distinctly.

b. Main Cuts

► Momentum

In the swarm of muons, there are many muons having low momentum. Such muons having low momentum have low energy also. So, muons having very low momentum are removed. It is difficult to assign the right value of momentum below which there are only low energy muons. However, when momentum is assigned to be greater than 400 GeV, the efficiency and purity of algorithm of finding high energy energy are optimized.

► Showers per Meter

The higher energy muons produce larger number of showers in the track. So, larger number of showers per unit length of the Detector indicates the high energy events.

► Rate of Loss of Energy

In the Detector, the muons lose energy. The lost energy is measured in the strips in the form of pulse height. The total pulse height per unit length of the Detector indicates energy loss per unit length. Larger rate of loss of energy indicates the high energy events.

► Standard Deviation of PH from MEU

Pulse Height (PH) measures the energy deposited by the muons on the Detector in unit MEU. The Muon Energy Unit (MEU) is defined, which corresponds to the energy deposited by an approximately 0.8 GeV muon passing perpendicularly through a 1 cm thick MINOS scintillator plane (the average absolute energy deposition by such a muon is approximately 2 MeV). An energy deposition of 1 MEU yields about 4 photoelectrons (PE) per strip-end [20]. The average energy deposited in the Far Detector is estimated to be 497.8 MEU. While the higher energy muons deposit larger amount of energy in the Detector , the lower energy muons deposit smaller. The standard deviation of the total PH from the average MEU is calculated. I have named this deviation as *MEUSD* and have defined as:

$$MEUSD = \frac{(Total\ PH - Average\ MEU)^2}{(Number\ of\ degree\ of\ freedom) \times (Average\ MEU)}$$

The larger magnitude of *MEUSD* should indicate the high energy muon events. The graph below shows the distribution of *MEUSD* for the Detector data.

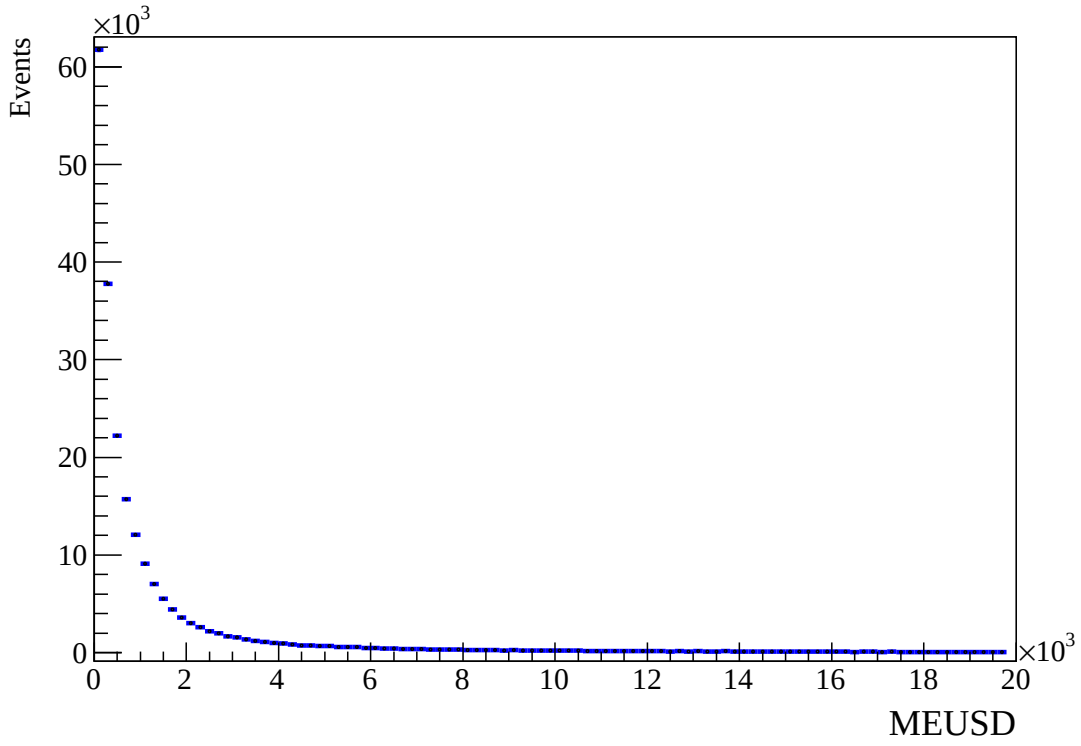

Figure 4.9: Distribution of MEUSD for the Detector data. A lot of high energy events are expected in the tail of the distribution

► Geometric Correction of PH

The geometry of the scintillator plays important role in the amount of energy deposited within it. The MINOS scintillators are 4.1 cm wide, 1 cm thick and up to 8 m in length (see Ch. 3). The scintillator is placed in the detector in such a way that the muons coming from the zenith travel through the width of 4.1 cm of the scintillator strip, while the muons coming through z-axis of the detector travel through only the thickness of 1 cm. The muons reaching the Detector come from a zenith angle of 0 to 90°. Modulus of the direction cosine of the z-axis (dcosz) of each muon track therefore lies in between 0 to 1. It is obvious that the muons passing through the scintillator at different angle cross different length of it. The more the length a particle travel within the scintillator strip, the more energy is deposited in the strip. So, the energy liberated by muons in the strip doesn't only depend on the energy of the incoming muons but also on the angle of the muons.

For low energy events (momentum < 200 GeV/c), average interval pulse height is plotted as a function

of dcosz. Where the interval is the chosen to be interval of 5 planes of the Detector. Such averaging of the PH over the 5 planes reduces fluctuations in the PH. The plot is polynomial fitted and parameters are recorded. This polynomial appears because of geometry of the Detector. So, it is to be deducted from the PH of high energy events to get rid of the geometrical effect. The histogram in Fig. 4.10 shows the distribution of the dcosz and Fig. 4.11 shows the corresponding distribution of PH for high energy events after applying the basic cuts.

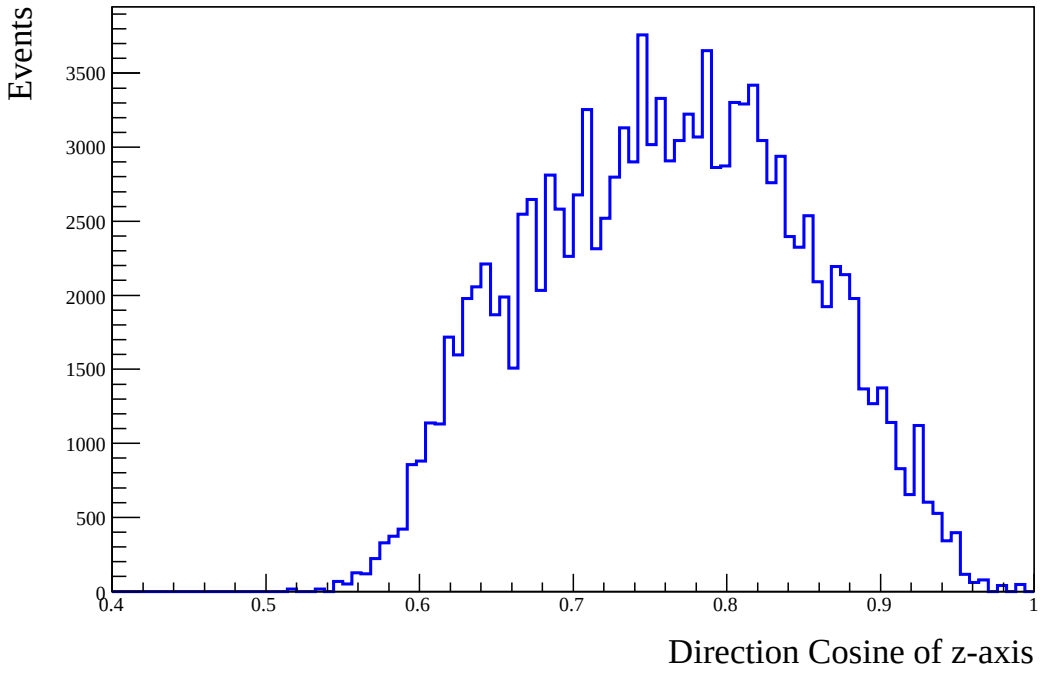

Figure 4.10: Distribution of direction cosine of z-axis. The distribution is after making basic selection cuts of MC data

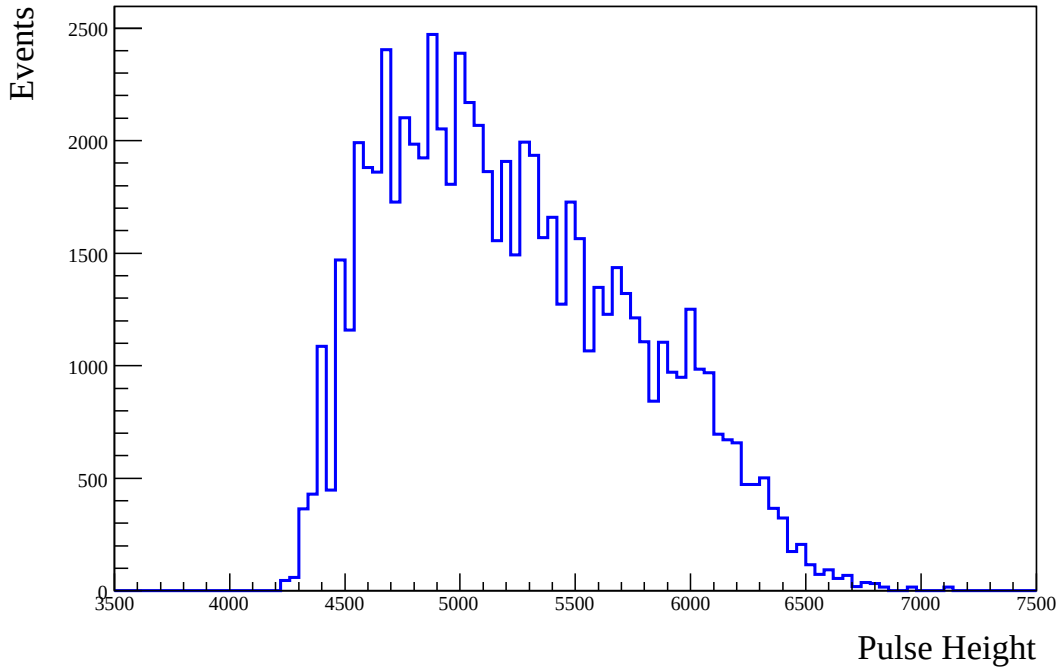

Figure 4.11: Distribution of Pulse Height corresponding to geometrical effect for high energy MC events

The distribution of PH events after deducting the distribution of PH appeared due to geometrical effect Fig. 4.11 is shown in Fig. 4.12. In the distribution the square of the positive difference per unit number of hits is included.

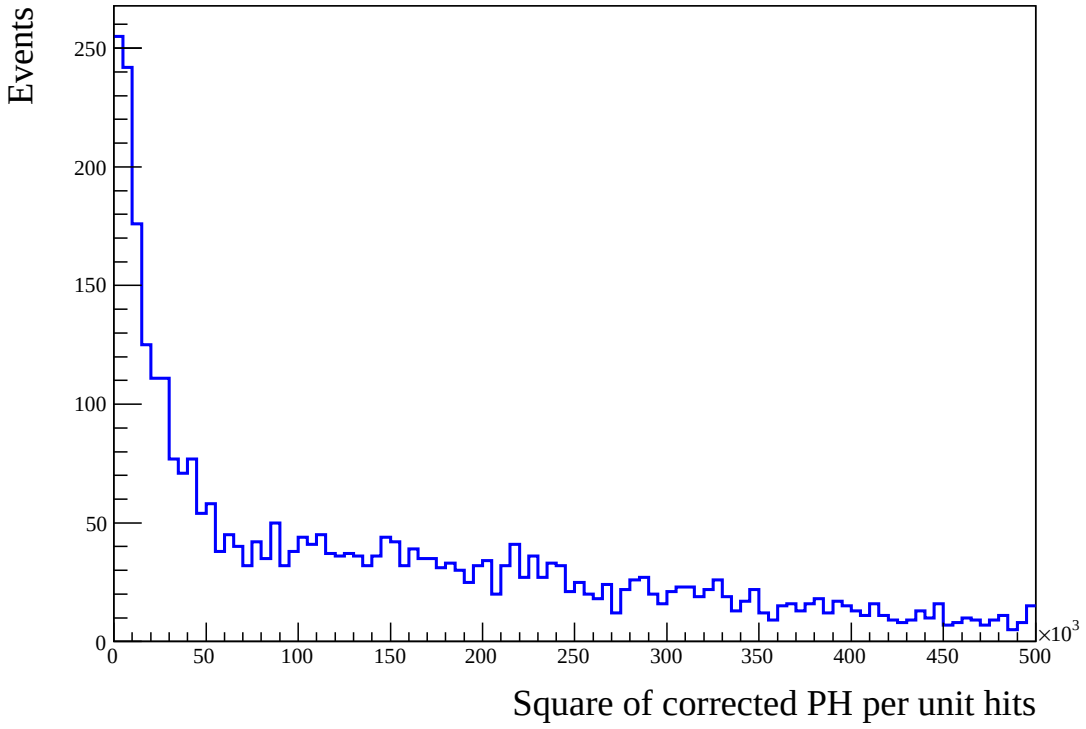

Figure 4.12: Square of positive difference of PH of MC data and the corresponding geometrical effect. A lot of radiative events are expected in the tail of the distribution.

The Table 4.1 shows the number of MC events survived after applying each cut. It shows that majority of events are uninteresting for present analysis.

Total Number of Events	104732	100%
Events Passed Track Cut ($= 1$)	100479	96% $*$
Events Passed Plane Cut (> 20)	100479	96% $*$
Events Passed Fiducial Cut (< 4.5 m)	100479	96% $*$
Events Passed Length Cut(>10 m) and Z-Distance Cut (> 2 m)	93619	89%
Events Passed Shower Cut (> 0)	82608	79%
Events Passed Curvature Cut ($< 1^\circ$)	63687	61%
Events Passed Momentum Cut (> 400 GeV/c)	13288	13%

Table 4.1: Number and fraction of events passed each cut for MC data. $*$Note that the data I used was already pre selected upto the Fiducial cut.So the percentage events passed through Track, Plane and Fiducial cut are same.

4.4 Signature of Radiative Loss

As a high energy muon passes through the Detector, it liberates its energy. The liberated energy is measured in each strip. The radiative loss of energy of muons occurs in the form of shower. If shower is produced a lot of PH is recorded in the strip near the location of shower. So, if the muons lose their energy through radiative methods then a drastic jump of PH is observed. The larger standard deviation of the PH indicates the larger loss of energy of the muons. The Fig. 4.13 show the measure of PH for a typical track of a muon. In the figure there are three large jumps in the magnitude of PH. The jumps indicate the showers and hence the radiative losses of the muons. This figure can correspond to the shower seen in Fig. 4.5.

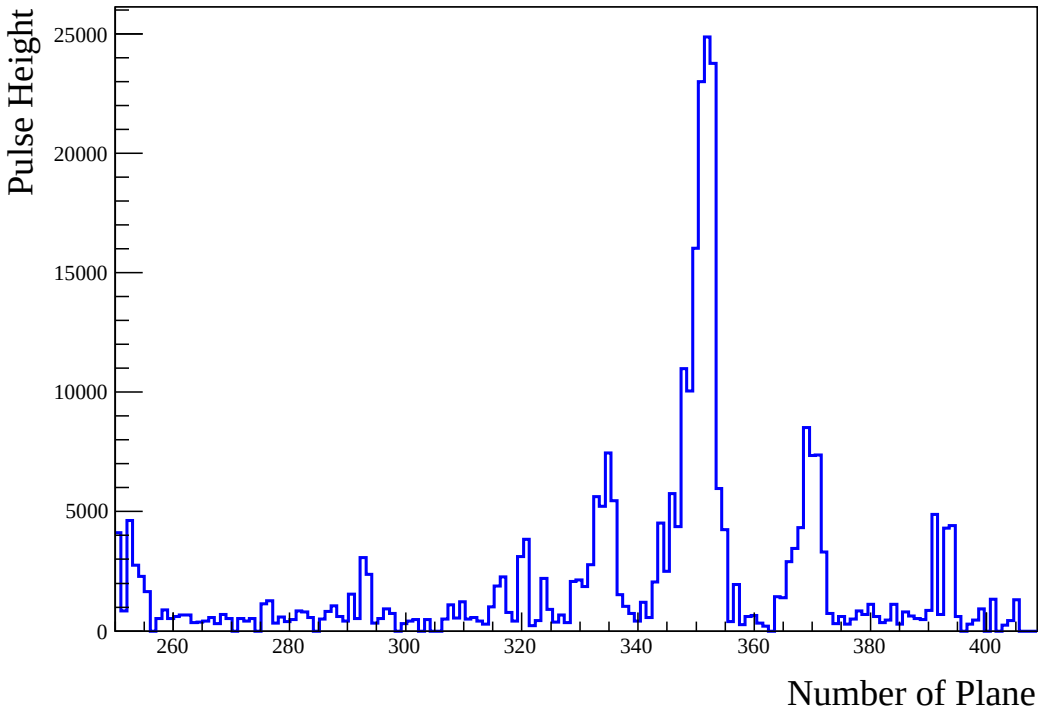

Figure 4.13: Distribution of PH as a typical muon track passes through different planes of the detector. There are prominent three showers at planes 330, 350 and 370.

The total PH in a track measures the total loss of energy of muons during the travel in the track. Its magnitude varies from small (about 0 MEU) to large value (more than 6000 MEU). In the Fig. 4.14, for the larger magnitudes of the PH in x-axis the larger number showering events are expected. For the distribution of PH before applying any selection cut, the RMS value of PH is 768 MEU.

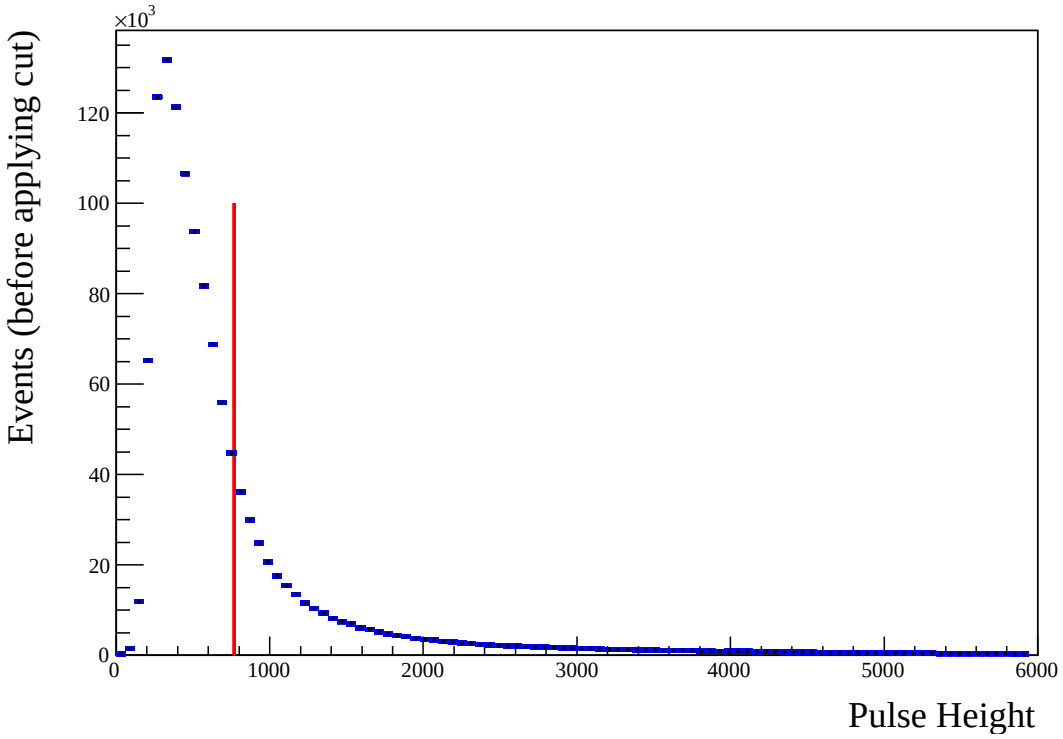

Figure 4.14: Distribution of PH before applying cut.The vertical red line is drawn at RMS value of PH at 768 MEU

As the selection cut is applied the most of the non-showering events are thrown away. So, the RMS value of the PH increases. In the Fig. 4.15 show the distribution of PH after applying selection cut. The RMS value of PH has reached to 1041 MEU.

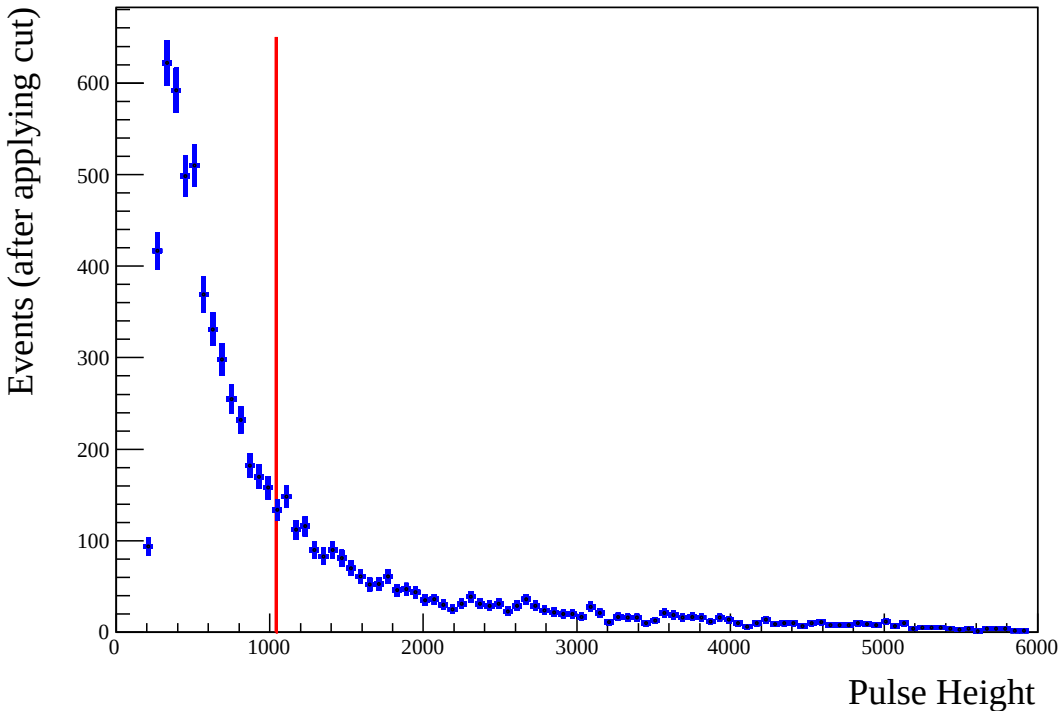

Figure 4.15: Distribution of PH after applying cut. The vertical red line is drawn at RMS value of PH at 1041 MEU

For further purity of high energy events cut on MEUSD can be applied. The graph 4.16 shows that the RMS value of PH increases as we increase the cut in MEUSD.

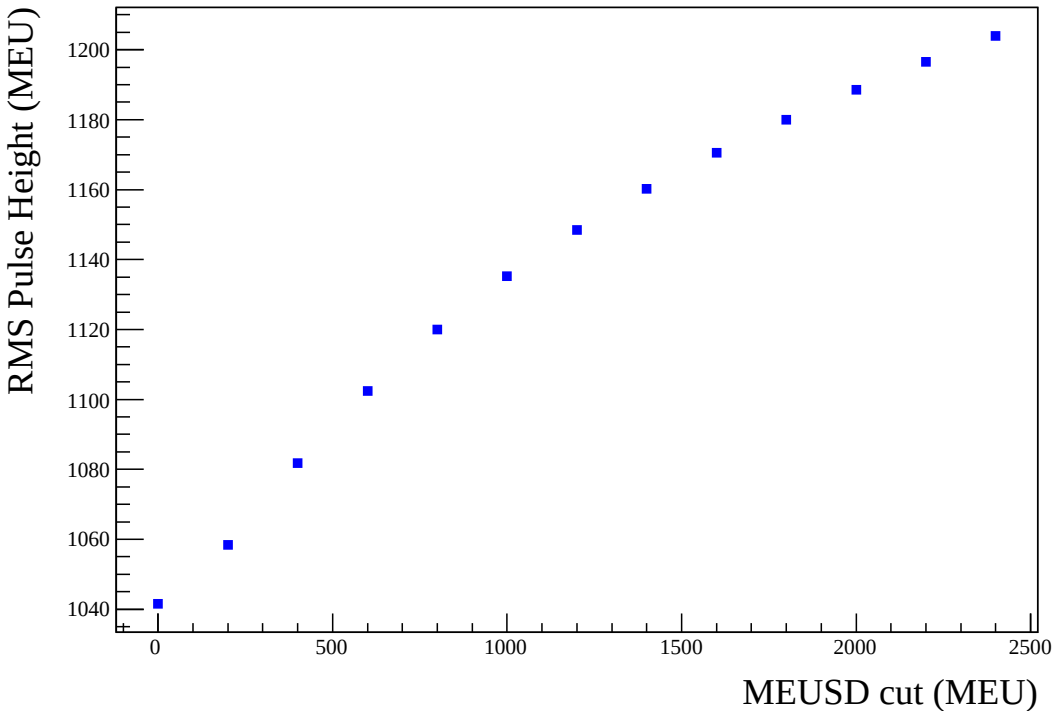

Figure 4.16: Root Mean Square (RMS) magnitude of distribution of Pulse Height (PH) increases as the MEUSD cut is increased from zero.

4.5 Comparison of Detector and MC data

To compare the MC data and the Detector data, fraction of events passing through the particular cut are seen. Here, the fraction is the ratio of number of events passed the cut to the total number of events. Theoretically the distribution of fraction should be similar. The Fig. 4.17 shows the fraction of the events passes length cut. The distribution of the fraction looks similar. However, the magnitude of the fraction do not match.

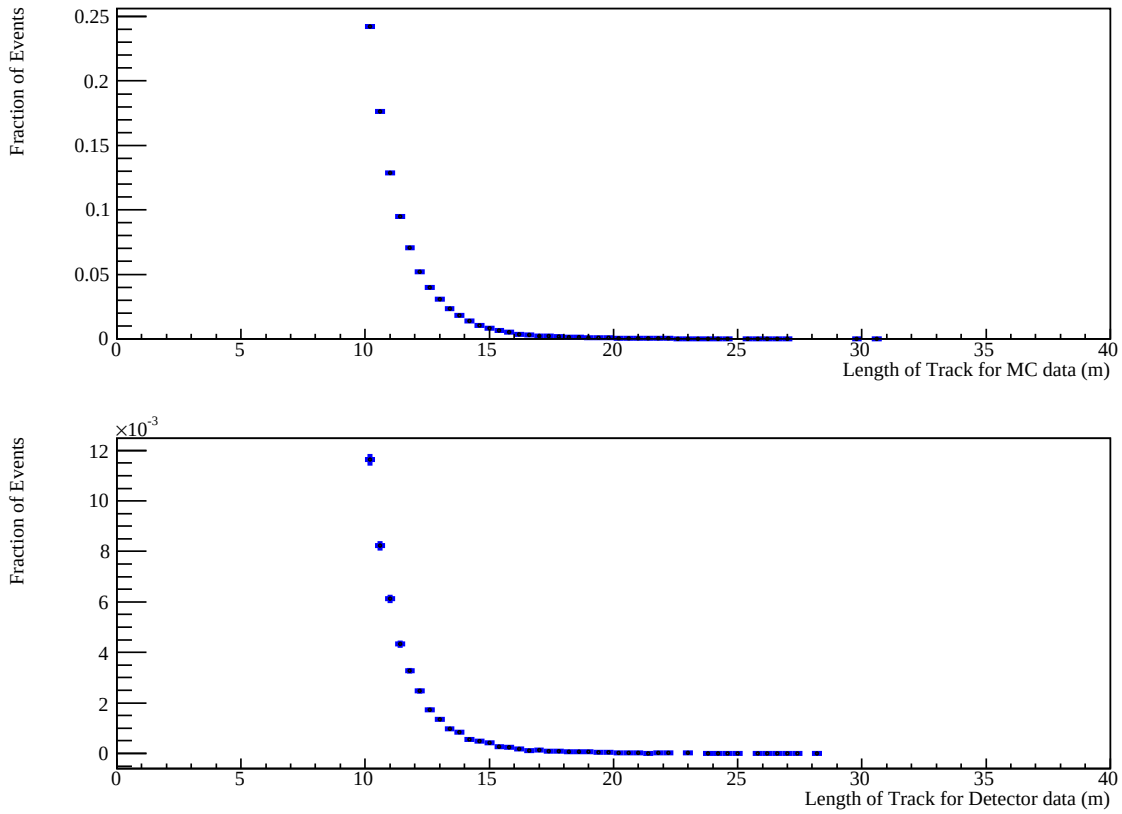

Figure 4.17: Comparison of lengths of track. The top graph is for MC data and the bottom one is for Detector data. It is seen that the distribution patterns of the length of track are similar. The error-bars are small to see.

The ratio of fraction of length of Detector and MC data is shown in Fig. 4.18. It is obtained by dividing the Detector data fraction by the MC data fraction of Fig. 4.17. For the perfect MC simulated data the ratio is expected to be unity.

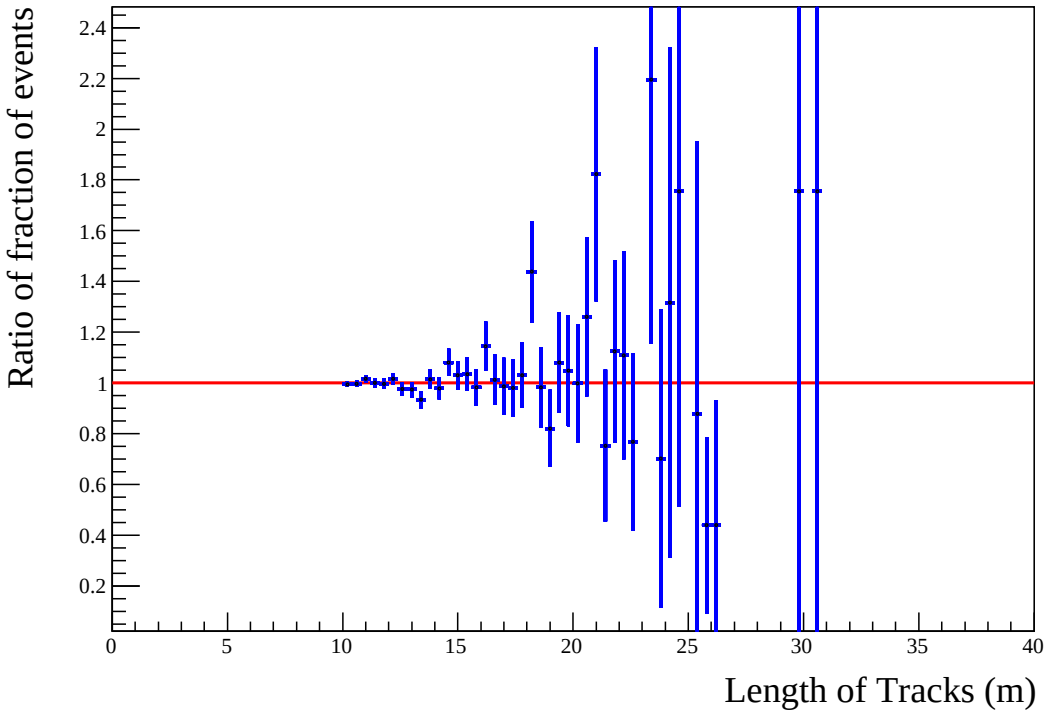

Figure 4.18: Ratio of fraction of length obtained from the Detector and the MC data Fig. 4.17. The red horizontal line is expected magnitude of the ratio. The error-bars indicate the statistical error. The ratio is close to expected ratio withing the error bar.

The fraction of data passed different curvature for both MC and Detector data events are shown in Fig. 4.19.

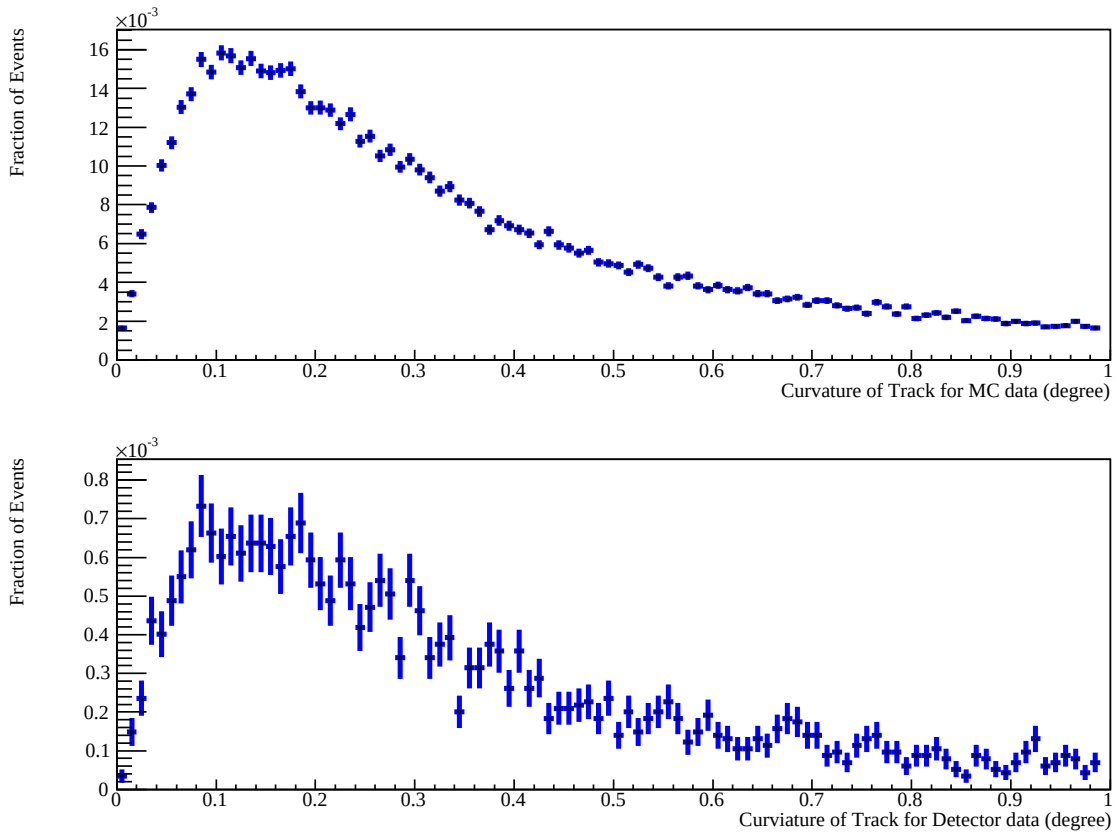

Figure 4.19: Fraction of data passed different curvatures. The top and bottom graph are for MC and Detector data respectively. The error-bars indicate the statistical error.

The ratio of histograms for MC and Detector data events in Fig. 4.19 is expected to be unity. However, the ratio is below unity.

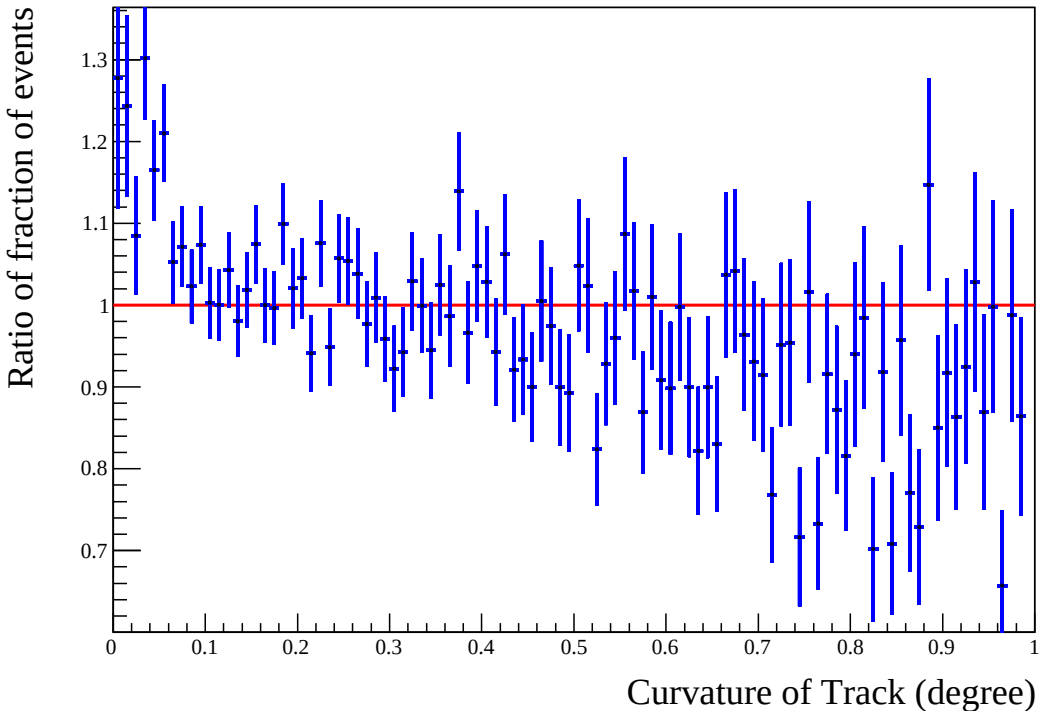

Figure 4.20: Ratio of the fraction histograms of MC and Detector data in Fig. 4.19. The expected ratio is drawn in red. The magnitude of the ratio well matches with the expected value of unity within the statistical error.

The fraction of momentum distribution is shown in Fig. 4.21. The distribution are similar.

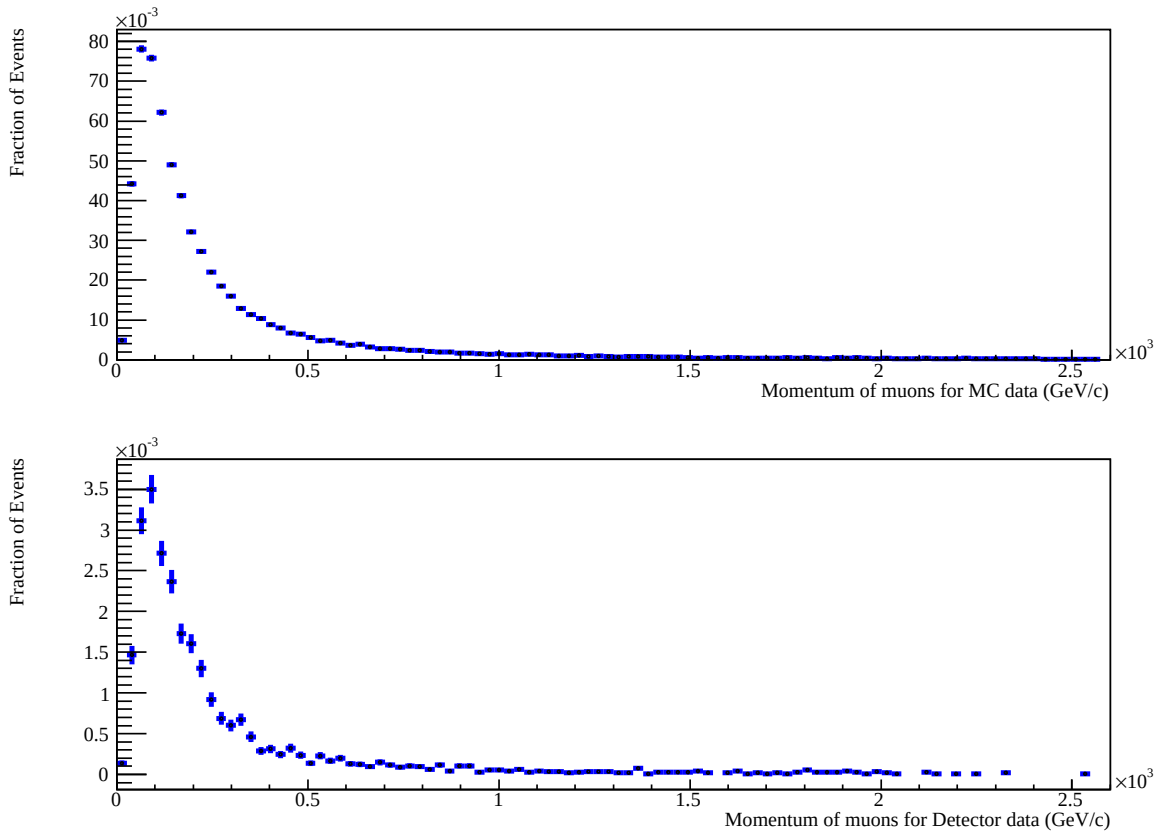

Figure 4.21: Fraction of events those passed different cuts of momentum for the MC data (top) and Detector Data (bottom). The error-bars indicate the statistical error.

The ratio of two distributions in Fig. 4.21 is shown in Fig. 4.22.

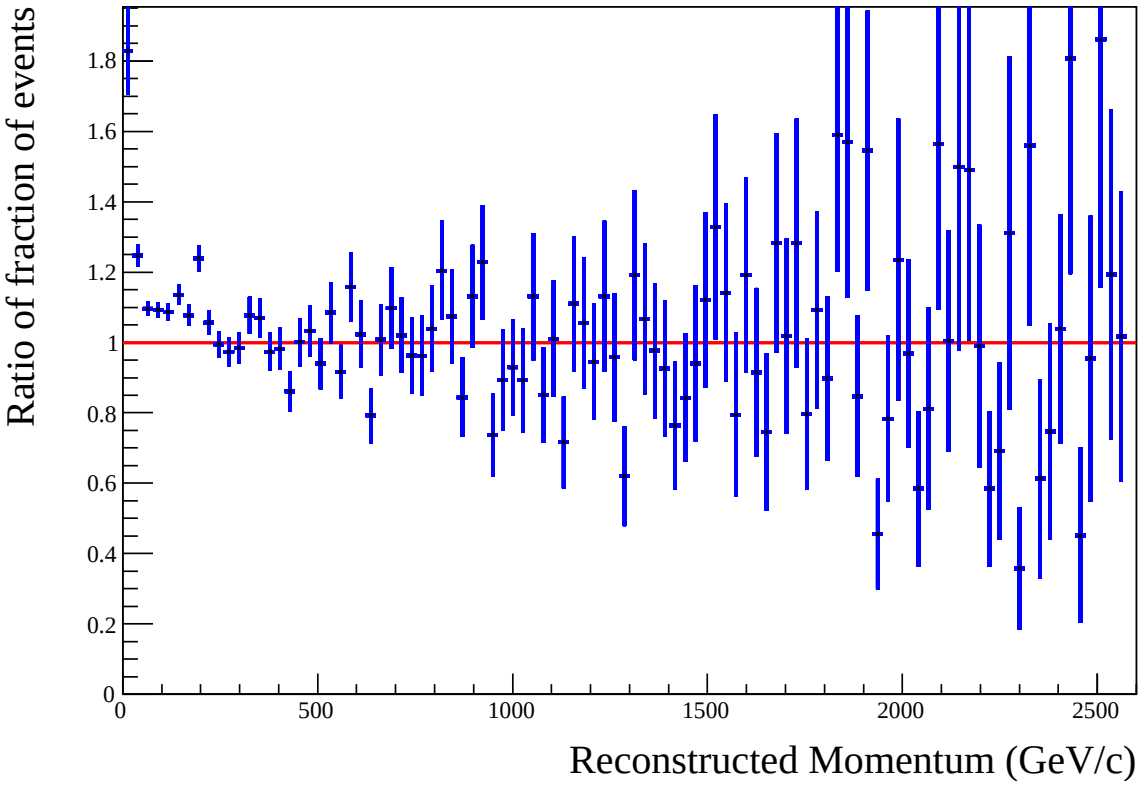

Figure 4.22: The double ratio distribution. It is the ratio of fraction of momentum of Detector data to MC data shown in Fig. 4.21. The red horizontal line passing through unity is the expected double ratio. The error-bars indicate the statistical error.

4.6 Summary of Data Analysis

Because of the stochastic nature of radiative energy loss of muons, it is hard to design a computing algorithm which selects radiative events with high purity and efficiency. My predecessors Steven Farrel and Eric Grashorn put some effort on writing algorithm to select radiative events of muons. Both of them worked for MC data. The algorithm written was efficient with efficiency and purity of 52 and 57% respectively. I put my effort on documentation of this work. Along with this, I compared the MC data with the Detector data. The MC data are good that its distribution matches with the distribution of the Detector data. The double ratio (ratio of fraction of events of Detector data to MC data) is very close to unity (see Fig. 4.20, 4.18 and 4.22).

However, the low value of efficiency and purity indicates that the improvement of the MC simulation algorithm is required.

Along with the comparison of MC and Detector data, I put my effort on updating NoNtple (see Sec. 4.2). The updated NoNtple is efficient with respect to time of computing and space of storage. It has number of variables those are essential for the analysis of cosmic muons in the MINOS Detectors.

Chapter 5

Conclusion

The cosmic ray MC data for the MINOS Far Detector has been studied to select the high energy muons those lose their energy through radiative methods such as pair-production, bremsstrahlung and photoproduction. In the selection process several cuts are applied. After making wise selection of cut, the high energy muons are selected. The computing algorithm of finding high energy muons is quite efficient with efficiency and purity 52 and 57% respectively (see Ch. 4). To answer the question whether the same cuts applied to the MC data are applicable to the Detector data, the distribution is the MC and Detector data has been analysed. The both data are found to be highly correlated with correlation coefficient 0.95 or more depending upon the variable selected for analysis. The double ratio plots in figures 4.20, 4.18 and 4.22 also show that the distribution of MC and Detector data are identical. So, the cuts applied in the MC data are applied and high energy muons are selected.

After conforming the similarity in different features of the MC and Detector data, I applied the cuts to the real data from the Detector. For analysis I took the Far Detector data of December 2004. I selected 6279 high energy muons out of 1299701 muons. For the analysis purpose I used the sample data of of one month only. For the applicatio purpose the MINOS Detetor data from 2003 to present can be used. The table 5.1 shows how many events passed each cut. As expected, few muons are of high energy.

Total Number of Events	1299701	100%
Events Passed Track Cut ($= 1$)	1153200	89%
Events Passed Plane Cut (> 20)	775518	60%
Events Passed Fiducial Cut (< 4.5 m)	773199	59%
Events Passed Length Cut (>10 m) and Z-Distance Cut (> 2 m)	53320	4.1%
Events Passed Shower Cut (> 0)	40555	3.1%
Events Passed Curvature Cut ($< 1^{\circ}$)	32621	2.5 %
Events Passed Momentum Cut (> 400 GeV/c)	6279	0.5%

Table 5.1: Number and fraction of events passed each cut for the Detector data.

The high energy muons are interesting for several project. The selection cut I decided are able to find a good sample of high energy cosmic muons from the MINOS Far Detector can be obtained. I have discussed in chapter 2 about the spectrum of muons. The spectrum follows the power law:

$$\frac{dN}{dE} = const \cdot E^{-\alpha}$$
$$N = const \cdot \left[E^{1-\alpha}\right]_{E'}^{\infty}$$

where N gives the number of muons having energy larger than $E^{'}$. For surface muons magnitude of α is -3.7 within 5% error [21]. Using the power law, the fraction of muons having energy higher than 400 GeV (which corresponds to the final cut of momentum 400 GeV/c) to the muons having energy higher than threshold energy (E_{th}). The E_{th} is 7 GeV which I found empirically from the distribution if momentum in the Detector data. It is the minimum energy of muon that crosses the track length of 10 m of the MINOS Detector.

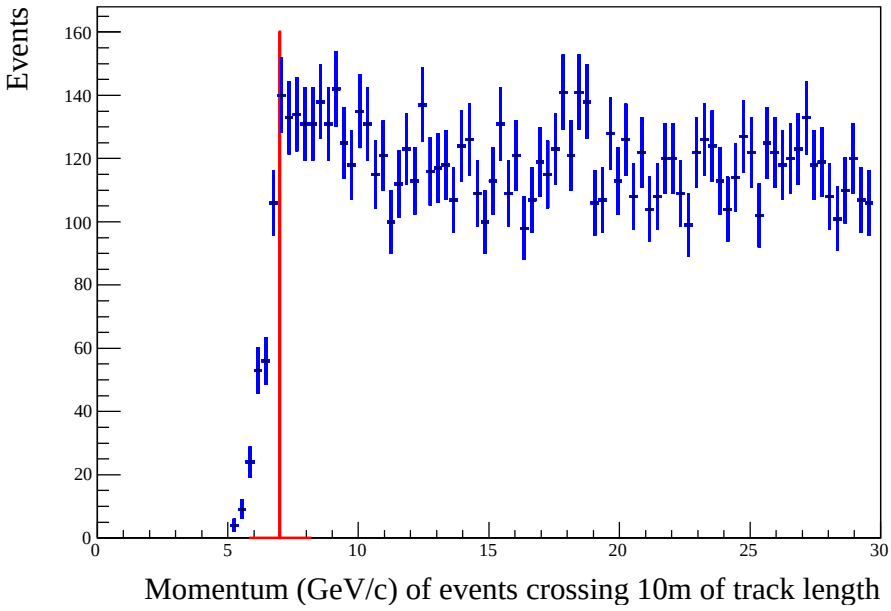

Figure 5.1: Distribution of the momentum of the Detector data. The red vertical line corresponds to the threshold energy of 7 GeV. The error bars are statistical.

$$Ratio = \frac{[N]^{\infty}_{E=400}}{[N]^{\infty}_{E=E_{th}}} = \left[\frac{400}{E_{th}}\right]^{1-\alpha}$$
$$= \left[\frac{400}{7}\right]^{1-\alpha}$$

This shows there is very small fraction (0.0018%) muons in the energy range beyond 400 GeV. Computing the fraction to the real Detector data and the MC data is in progress.

This analysis techniques of finding high energy muons can be used in several projects. High energy cosmic rays move in almost straight line. Sun or moon lying on their path casts shadow. High energy muons are used in sum moon shadow studies [1]. Thus, study of such high energy muons obtained from my analysis help to study cosmic ray point sources. Also, typical reactions in stratosphere during the production of high energy muons help us to study and understand stratosphere. The high energy muons obtained from my analysis help in this purpose. Similarly, high energy muons can be used to study cosmic ray primary interactions [22] [23].

Bibliography

[1] Eric W. Grashorn. Astroparticle physics with the MINOS far detector. *Ph.D. thesis, University of Minnesota(2008)*, 2008.

[2] Seth H. Neddermeyer and Carl D. Anderson. Note on the nature of cosmoc-ray particles. *Phys. Rev.*, 51:884–886, 1937.

[3] T. K. Gaisser. *Cosmic Rays and Particle Physics*. Cambridge University Press, Cambridge, UK, 1990.

[4] Alec T. Habig. Muon astronomy and cosmic ray physics with the MACRO detector. *Ph.D. thesis, Indiana University*, 1996.

[5] Kanetada Nagamne. *Introductory Muon Science*. Cambridge Univ. Pr., 2003.

[6] Peter K. F. Grieder. *Cosmic Rays at Earth : Researcher's Reference Manual and Data Book*. Elsevier Science B.V, Amsterdam, Netherland, 2001.

[7] E. Haug and W. Nakel. The elementary process of bremsstrahlung. *World Scientific Lecture Notes in Phys*, 73, 2004.

[8] Yung-Su Tsai. Pair Production and Bremsstrahlung of Charged Leptons. *Rev. of Mod. Phys*, 46:815–851, 1974.

[9] David H. Frisch and James H. Smith. The measurement of the relativistic time dialation using μ-mesons. *American Journal of Physics*, 31:342–355, 1963.

[10] Various. Physics letters b. *Review of Particle Physics*, 667:267–279, 2008.

[11] Todor Stanev. *High Energy Cosmic Rays*. Praxis Publising Ltd., Chichester, UK, 2004.

[12] R. A. Dunlap. *Experimental Physics Modern Methods*. Oxford Univ.Pr., 1988.

[13] P. Adamson et al. The MINOS scintillator calorimeter system. *IEEE Trans. Nucl. Sci.*, 49:861–863, 2002.

[14] D. G. Michael. The magnetized steel and scintillator calorimeters of the MINOS experiment. *Nuclear Instruments and Methods in Physics Research A*, 596, 2008.

[15] D. Jason Koskinen. An Overview of the Main Injector Neutrino Oscillation Search, the Rack Protection System, and Methods to Degauss a Large Iron Calorimeter Particle Detector. Master's thesis, University of Minnesota, Duluth, 2004.

[16] The MINOS Collaboration. The MINOS technical design report. Technical report, Fermilab, oct 1998.

[17] Philip R. Bevington and D. Keith Robinson. *Data Reduction and Error Analysis for Physical Sciences*. Mc Graw Hill Inc., NY, USA, 2003.

[18] R. Brun and F. Rademakers. Root: An object oriented data analysis framework. *Nucl. Instrum. Meth.*, A389:81–86, 1997.

[19] Bjarne Stroustrup. *The C++ Programming Language*. Addison-Wesley, third edition, 1997.

[20] A Cabrera et.al. Comparision of the minos near and far detecror readout systems at a test beam. *Nuclear Instruments and Method in Physics Research A*, 609:106–113, 2009.

[21] M. Ambrosio et. al. Measurement of the residual energy of muons in the Gran Sasso underground Laboratories. 2002.

[22] E. W. Grashorn et al. The atmospheric charged kaon/pion ratio using seasonal variation methods. *Astropart. Phys.*, 33:140–145, 2010.

[23] S. Osprey et al. Sudden stratospheric warmings seen in MINOS deep underground muon data. *Geophys. Res. Lett.*, 36:L05809, 2009.